Surface deformation and tectonic setting of Taiwan inferred from a GPS velocity field

Annemarie G. Bos and Wim Spakman

Faculty of Earth Sciences, Utrecht University, Utrecht, Netherlands

Marleen C. J. Nyst[1]

Delft Institute of Earth Oriented Space Research, Delft University of Technology, Delft, Netherlands

[1] We have determined the present-day surface deformation of Taiwan by computing the velocity gradient field and fault slip from 143 GPS velocity vectors. In southern Taiwan the derived strain and rotation rates and fault slips are indicative of lateral extrusion toward the south. In northern Taiwan we infer the onset of gravitational collapse which is induced by the on-land extension of the Okinawa Trough. In the eastern Central Range the observed inverted NW-SE extension is consistent with geological observations and high heat flow measurements. This could be the result of exhumation of crustal material. The model further shows a significant decrease in slip rate northward along the Longitudinal Valley fault at 23.7°N. The northern Coastal Range shows high strain rates and two oppositely rotating blocks. By combining the surface deformation model with seismicity data and seismic tomography we are able to propose a coherent model for the present-day tectonic activity. Both seismicity and tomography show further evidence for active, southward propagating exhumation of a crustal slice in the eastern Central Range. Offshore east Taiwan we deduce strong evidence of a southward propagating crustal tear fault, accommodating most of the Philippine Sea Plate-Eurasian Plate convergence. The tear is the crustal response to incipient northwestward subduction of the Philippine Sea Plate. Thus the Ryukyu Trench is bending southward becoming almost perpendicular to the convergence direction, while subduction of the Philippine Sea Plate continues. In this setting a sudden rapid southward propagation of the afore mentioned tear is conceivable. *INDEX TERMS:* 1208 Geodesy and Gravity: Crustal movements—intraplate (8110); 8110 Tectonophysics: Continental tectonics—general (0905); 9320 Information Related to Geographic Region: Asia; *KEYWORDS:* tectonic setting, GPS data, Taiwan, surface deformation

1. Introduction

[2] The island of Taiwan is a zone of active continental deformation located in an exceptional tectonic setting within the plate boundary zone between the Eurasian Plate (EUP) and the Philippine Sea Plate (PSP) (Figure 1). At Taiwan the PSP is moving toward the EUP at a rate of 70–80 mm yr^{-1} in the direction N306°E [*Seno et al.*, 1993] (inset of Figure 1). The complexity of Taiwan's tectonic setting arises from the fact that at the Ryukyu Trench the PSP subducts north-northwestward underneath the EUP, whereas at the Manila Trench the PSP overrides the EUP in a westward direction. Taiwan is located at the transfer zone between subduction and overriding of the PSP. The 150 km long, NNE trending Longitudinal Valley Fault (LVF) on the island of Taiwan is generally considered as the suture zone between the two plates [*Barrier and Angelier*, 1986; *Biq*, 1972] accounting for 25–30% of the total plate convergence [*Angelier et al.*, 2000].

[3] The still ongoing collision between the Luzon volcanic arc and the Chinese continental margin started at least 8 Myr ago [*Ho*, 1988; *Kao et al.*, 1998; *Lallemand et al.*, 2001; *Teng*, 1990] thereby creating and building the Taiwan orogen. Because of the oblique orientation of the strike of the arc relative to the strike of the passive margin, the collision at Taiwan has migrated southward, incorporating ever new portions of the Luzon arc [*Lewis and Hayes*, 1983; *Suppe*, 1981]. Details of the geodynamic evolution and present-day tectonic setting of Taiwan are by no means resolved. This becomes evident from the variety of contradicting models proposed in the literature [*Angelier et al.*, 1990; *Chemenda et al.*, 1997; *Lu and Malavieille*, 1994; *Suppe*, 1981; *Teng*, 1990; *Wu et al.*, 1997].

[4] These models focus on two closely related processes: the geometry and dynamics of the transition between the

---

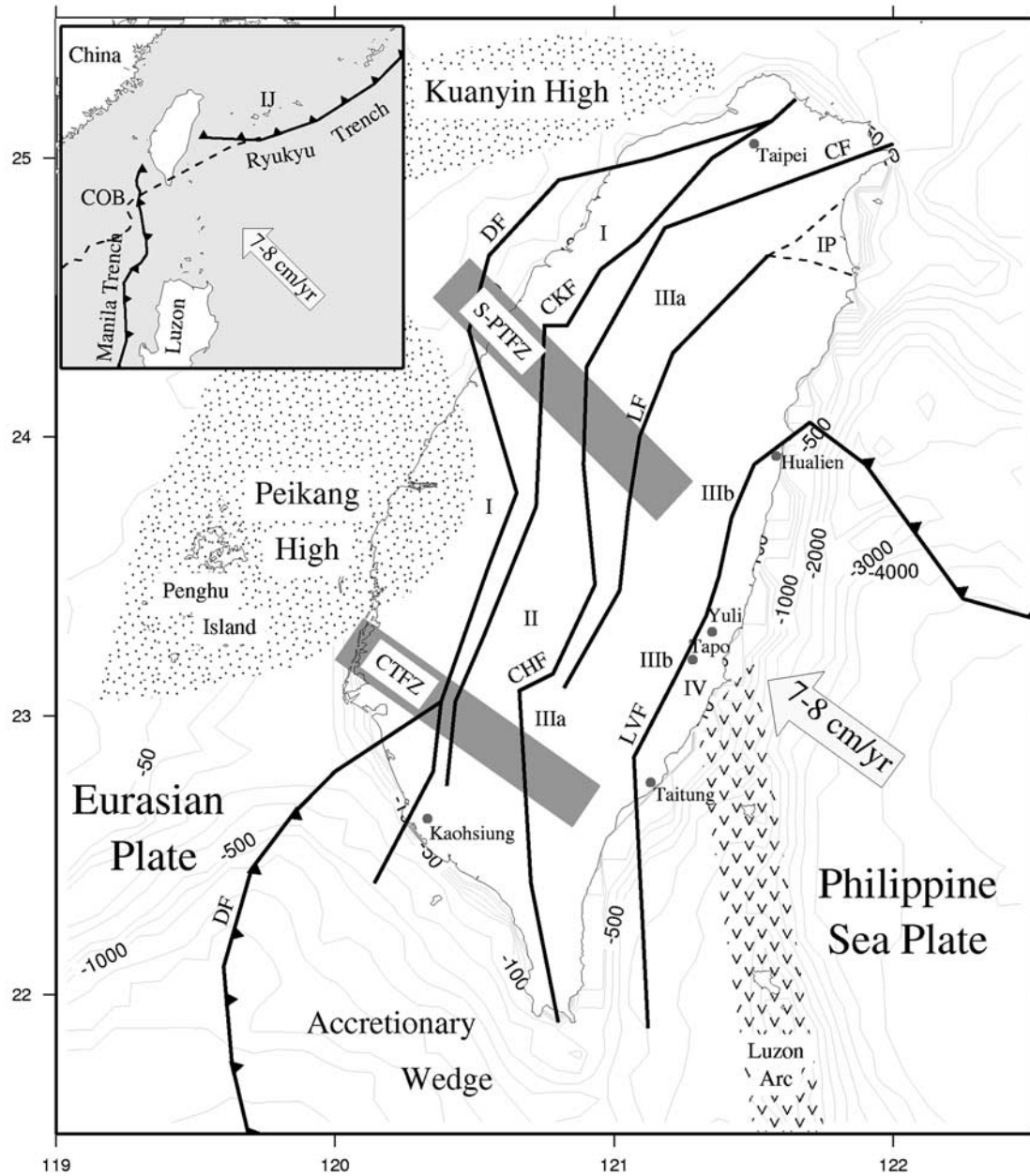[1]Now at U.S. Geological Survey, Menlo Park, California, USA.

Figure 1. Tectonic setting of Taiwan showing major faults as used in this study: LVF, Longitudinal Valley Fault; LF, Lishan Fault; CF, Chuchin Fault; CHF, Chaochou-Chishan Fault; CKF, Chukou Fault; DF, Deformation Front, and the main geological provinces: I, Coastal Plain; II, Western Foothills (WF); IIIa, western Central Range (WCR); IIIb, eastern Central Range (ECR); IV, Coastal Range (CoR); IJ, Ishigaki-Jima; IP, Ilan Plain; and COB, continent-ocean boundary.

two subduction zones and the evolution of the Taiwan orogen. The hypothesis of the ''thin-skinned'' or ''critical taper'' model [*Barr and Dahlen*, 1990; *Dahlen*, 1990] for actively deforming fold-and-thrust belts has been challenged by models including the basement of the crust in the mountain building process [*Ellwood et al.*, 1996; *Hwang and Wang*, 1993; *Wu et al.*, 1997]. In the thin-skinned models, active deformation is confined to a trapezoidal segment of a wedge overlying a planar decollement fault, whereas the ''basement involved'' models require the discrete incorporation of autochthonous basement material into

the shallow parts of the orogen. A model of crustal subduction followed by exhumation [*Chemenda et al.*, 2001; *Lin*, 1998; *Lin et al.*, 1998] has also been proposed to explain the rapid uplift and high heat flow in the Central Range of Taiwan (Figure 1). *Lallemand et al.* [1997, 2001] and *Teng et al.* [2000] propose detachment of the Eurasian slab beneath Taiwan as a mechanism to create space for the subduction of the PSP slab along the westward propagating Ryukyu trench. Analogue modeling has shown the possibility of subduction reversal along a boundary comparable to the LVF of Taiwan in a similar setting of two contrary

subduction zones, as well as provided insight in the mechanisms behind the processes of exhumation and lateral extrusion [*Chemenda et al.*, 1997, 2001; *Lu and Malavieille*, 1994]. These and other models still require further testing against available geological, geophysical and, in particular, geodetic data acquired in the past decade.

[5] In 1989 the "Taiwan GPS Network" was established by the Institute of Earth Sciences, Academica Sinica (IESAS). On the basis of the 1990–1995 data of the network, *Yu et al.* [1997] derived the present-day velocity field of the Taiwan area. Such a velocity field provides significant information on the kinematics of the crustal deformation. We apply the inversion method of *Spakman and Nyst* [2002] to the GPS velocity field of *Yu et al.* [1997] in order to determine the kinematic properties of the surface deformation. This method solves simultaneously for the velocity gradient field and fault slip. The *Spakman and Nyst* [2002] method utilizes a physical relation between the velocity gradient field, fault motion and the relative velocity data which is significantly different from similar studies on complicated regions which are based on spatial interpolation of the data [e.g., *Beavan and Haines*, 2001; *Wdowinski et al.*, 2001]. The incorporation of fault slip in a joint inversion with the velocity gradient field is a unique characteristic of the method. In contrast to for instance elastic dislocation modeling [e.g., *Bennett et al.*, 1996], our method requires no assumptions on crustal or fault dynamics (see *Spakman and Nyst* [2002] for further discussion). From the velocity gradient tensor we easily obtain the strain rate and rotation rate tensor fields. In conjunction with geological observations in the area, we interpret the obtained surface deformation model in terms of the kinematics of crustal processes. By combining the surface deformation model with seismicity data and seismic tomography we are able to propose a coherent model for the present-day tectonic activity at the island of Taiwan.

2. Geologic Setting

[6] Geologically, Taiwan can be divided into four N-NE trending provinces which are separated by active faults (Figure 1). The provinces compose a west vergent collisional prism involving both the Chinese continental margin and the Luzon Arc. In the eastern Central Range (ECR), pre-Tertiary high-grade metamorphic rocks of the Chinese margin are exposed, while the Coastal Range (CoR) is composed of Neogene andesitic volcanic units of the northern Luzon Arc [*Yu et al.*, 1997; *Hu et al.*, 1996].

[7] The general structural trends of the Taiwan mountain belt show an elongated S shape (Figure 1). Southern Taiwan is dominated by the onshore extension of the Manila accretionary wedge, representing a particular zone of weakness related to the northern part of the Manila subduction system. To the north of this region, the accretionary wedge is terminated by the Chishan Transfer Fault zone (CTFZ), which appears as a major structural, seismological and kinematic boundary trending N130°E [*Lacombe et al.*, 2001]. Another major wrench fault zone cutting across Taiwan is the Sanyi-Pakua Transfer Fault Zone (S-PTFZ). This N140°E trending left-lateral fault zone is also accompanied by high seismicity and offsets several major struc-
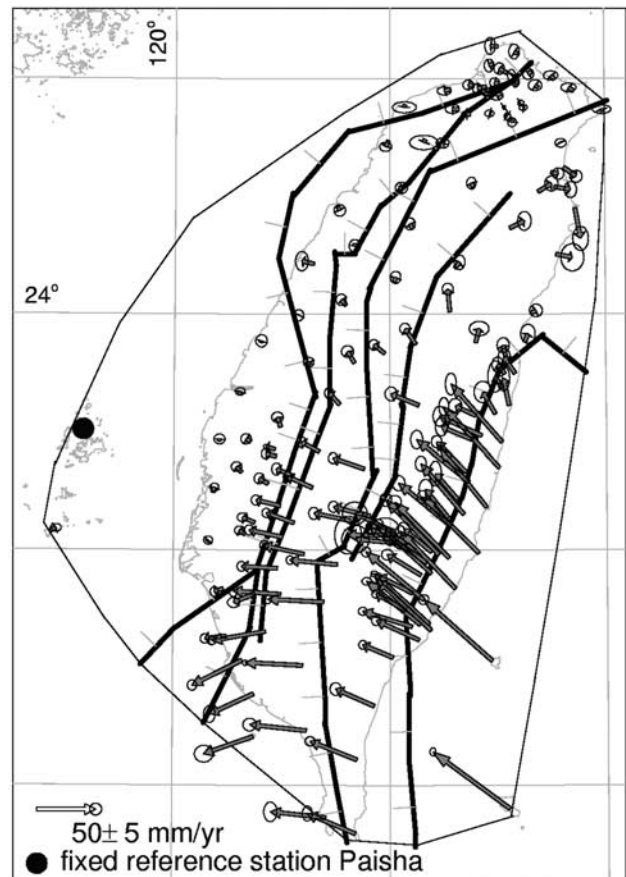

Figure 2. GPS velocity vectors of Taiwan [*Yu et al.*, 1997] as used in this study with their 95% confidence error ellipses.

tures [*Deffontaines et al.*, 1997]. The prominent Peikang and Kuanyin High represent the shallow pre-Cretaceous Chinese continental basement. They are accompanied by significant Bouguer anomalies [*Hsieh and Hu*, 1972] and are characterized by tectonic stability. The deformation front (DF) is located along the western edge of the accretionary wedge in the south and progresses north through the Coastal Plain (CP) along the eastern edges of the basement highs. Generally, all deformation related to the convergence of the PSP and EUP is considered to be accommodated east of the DF (Figure 1).

3. GPS Data

[8] In our modeling, we use the data set of GPS motion vectors published by *Yu et al.* [1997]. These vectors are determined for 131 stations of the Taiwan GPS Network that were surveyed 4–6 times between 1990 and 1995, four continuously recording stations and five semipermanent stations (Figure 2). In the calculation of the station velocities, *Yu et al.* [1997] chose the Paisha station (S01R), situated at the relatively stable Chinese continental margin, as the fixed reference station and fixed the azimuth from Paisha to Taipei (at 52.1°) to resolve the translational and rotational ambiguities of the whole network in the estimation. We adopt this reference station for plotting purposes, but note that our analysis is independent of reference frame.
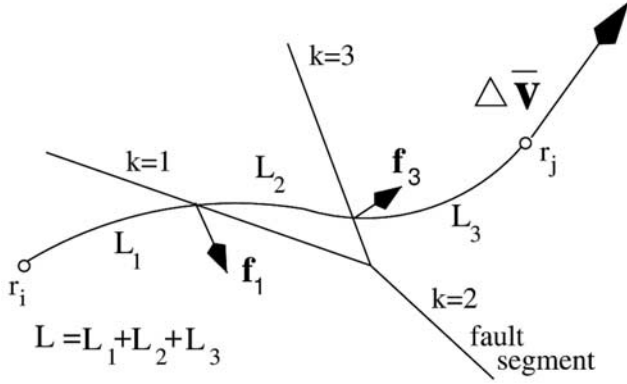
Figure 3. Forward problem of relating relative velocity to the velocity gradient field and fault slip. The curved path L_{ij} connects two observation sites i and j with relative motion Δv_{ij}.

[9] Several earthquakes with magnitude 5.0 or more occurred in or near the area of observation during the time of observation. However, since they did not have a significant effect on the length changes of the baselines, steady state motion is assumed during the period of observation [*Yu et al.*, 1997].

4. The Spakman-Nyst Method

[10] We use the inversion method of *Spakman and Nyst* [2002] to determine the surface deformation of Taiwan in terms of discrete movements along faults (creep/slip) and continuous deformation in crustal blocks from relative motion data. The kinematic method does not require any assumptions about the dynamics causing the deformation or the rheology of the crust. For stationary deformation the method relates the observed relative motion ($\Delta \mathbf{v}_{ij}$) between station i and station j to the velocity gradient field ($\nabla \mathbf{v}$) and fault slip ($\mathbf{f}_k$) on fault segment k (Figure 3):

$$\Delta \mathbf{v}_{ij} = \sum_{l=1}^{K+1} \int_{L_{ij}^l} \nabla \mathbf{v}(\mathbf{r}) \cdot d\mathbf{r} + \sum_{k=1}^{K} \alpha_k \mathbf{f}_k \left(r_{ij}^k \right), \quad (1)$$

where L_{ij}^l is the integration path connecting stations i and j. K denotes the number of crossed fault segments, $\alpha_k = \pm 1$ depends on the fault orientation with respect to the direction of integration along path L_{ij}^l, $\mathbf{f}_k$ is the slip rate on fault k at the intersection r_{ij}^k between L_{ij}^l and the fault, and $\nabla \mathbf{v}(\mathbf{r})$ is the velocity gradient tensor.

[11] The first part of the right-hand side of equation (1) denotes the contribution of continuous deformation to the relative motion between the two stations. The integration over the $\nabla \mathbf{v}$ is done in parts, since the $\nabla \mathbf{v}$ can be discontinuous across slipping/creeping faults. The symmetric part of the velocity gradient tensor constitutes the strain rate field, where the antisymmetric part constitutes the rotation rate field. The second part represents the motion due to fault slip on K faults crossed by a path L_{ij}^l. Equation (1) is purely linear in the unknown quantities $\nabla \mathbf{v}$ and $\mathbf{f}_k$ and offers a complete description of the relative crustal motion Δv_{ij} resulting from stationary crustal deformation.

[12] A set of M geodetic relative motion observations yield at least $M(M - 1)/2$ vector equations (1) coupled through $\nabla \mathbf{v}$ and $\mathbf{f}_k$. We divide the faults into segments and for each segment the relative fault slip rate $\mathbf{f}_k$ is parameterized as a (segment dependent) constant rate. The study region is subdivided into a network of N nodes connected by triangulation with the restriction that triangles cannot intersect with faults. We adopt a linear behavior of the velocity gradient (quadratic displacement) on the spatial coordinates in each triangle [*Spakman and Nyst*, 2002]. This model parameterization is basically the only assumption entering the observation equation (1) and is used to arrive at a linear matrix system of equations. The density of the station distribution in the model area is used as a guide for local densification of the grid. We include the surface traces of "major," active faults. The "minor" faults are implicitly represented by the velocity gradient field. We do not attempt to incorporate all known faults, since the current data density is insufficient to independently resolve the velocity gradient field and slip/creep on numerous minor faults in such a more detailed parameterization.

[13] Substitution of the parameterization in equation (1) yields an ordinary set of coupled equations, which can be assembled in a matrix-vector form (see *Spakman and Nyst* [2002] for details). Since the relative motion between 2 points is independent of the choice of L_{ij}^l, the matrix system can be extended with more data equations using the same observation set Δv_{ij}. Closed integration paths ($L_{ij}^l - L_{ji}^l$) between stations i and j will always render zero relative motion; therefore the closed paths which only sample continuously deforming crust are effectively replaced by the local constraint that $\nabla \times \nabla \mathbf{v} = \mathbf{0}$. Additional paths L_{ij}^l may be required across faults to ensure internal consistency between fault slip and the velocity gradient field. This effectively leads to an extended set of data equations. Data errors, nonuniqueness and ill-conditioning of the observation matrix cause our matrix-vector system to be an inconsistent set of equations. To deal with problems associated with this, we adopt an inversion scheme which selects a solution that fits the data in a least squares sense and at the same time minimizes some model norm. On the basis of the characteristics of the model area (e.g., station density) we adopt a combination of amplitude damping on the boundary of the modeling area and, in the model interior, amplitude damping combined with spatially varying first derivative regularization. The model minimizing the data residual and the adopted model norm (defined by the regularization) is given by [*Spakman and Nyst*, 2002]

$$\mathbf{m} = \left(\mathbf{A}^T \mathbf{C}_d^{-1} \mathbf{A} + \alpha_0^2 \mathbf{I}_b + \alpha_1^2 \mathbf{I}_g + \alpha_2^2 \mathbf{D}_1^T \mathbf{D}_1 \right)^{-1} \mathbf{A}^T \mathbf{C}_d^{-1} \hat{\mathbf{d}}, \quad (2)$$

with a posteriori model covariance given by $\mathbf{C} = (\mathbf{A}^T \mathbf{C}_d^{-1} \mathbf{A} + \alpha_0^2 \mathbf{I}_b + \alpha_1^2 \mathbf{I}_g + \alpha_2^2 \mathbf{D}_1^T \mathbf{D}_1)^{-1}$ and model resolution kernel $\mathbf{R} = \mathbf{C} \mathbf{A}^T \mathbf{C}_d^{-1} \mathbf{A}$. Here $\mathbf{A}$ represents the coefficient matrix, $\hat{\mathbf{d}}$ is the observed velocity data vector including the $\nabla \times \nabla \mathbf{v} = \mathbf{0}$ constraints, and $\mathbf{C}_d$ denotes the data covariance matrix. Since our data vector $\mathbf{d}$ consists of all $M(M - 1)/2$ relative velocities, our data covariance matrix $\mathbf{C}_d$ would obtain dimensions $M(M - 1)/2$ by $M(M - 1)/2$. Inversion of this matrix would be very impractical, if not impossible. Therefore we only utilize the data standard deviations, which through standard error propagation results in the standard

deviation vector for the data vector $\hat{\mathbf{d}}$. $\mathbf{I}_b$ and $\mathbf{I}_g$ are identity matrices for the boundary and general damping, respectively, and $\mathbf{D}_1$ stands for the first derivative operator. α_0, α_1 and α_2 are the weighting factors of the amplitude damping and first derivative regularization equations and control the trade-off between fitting the data and minimizing the weighted model norm. The inversion depends on four tuning parameters: the weight (α_r) attributed to the surface constraint $\nabla \times \nabla \mathbf{v} = \mathbf{0}$, the weight α_0 for the boundary node damping, the weight α_1 for the amplitude damping in the interior of the model and the weight α_2 attributed to the first derivative operator. We investigate a range of solutions obtained with different combinations of the tuning parameters.

[14] For the analysis of the inversion results we define the model normalized χ^2 per degree of freedom:

$$\chi_v^2 = \frac{1}{v} \sum_{i=1}^{N} \frac{e_i^2}{\sigma_i^2}, \quad (3)$$

where N are the number of data equations, M is the number of model parameters, $v = N - M$ is the degrees of freedom of the model, $e_i = d_i^{\mathrm{obs}} - d_i^{\mathrm{pre}}$ is the prediction error of the model and σ_i^2 is the 1σ data variance. For models with a high degree of freedom a proper data fit will result in a χ^2 of around one. A $\chi^2 \gg 1$ indicates that we are unable to fit the data with the current model, whereas a $\chi^2 \ll 1$ identifies an attempt to model the data error, and may imply more model detail than supported by the data signal. The χ^2 determination is, however, completely dependent on the data error: An overestimation of such an error may result in a χ^2 which is significantly smaller than 1 and vice versa. Further, we use $\tilde{\sigma}_m = 1/M \sum_{i=1}^{M} \sqrt{C_{ii}}$ as an average indication of the model error.

5. Inversions

[15] The *Spakman and Nyst* [2002] method provides the possibility to solve for three different types of models for surface deformation. The first application (I) only solves for the fault slip vectors, hence assuming the crustal deformation field to be only controlled by motion/creep on unlocked, freely slipping faults; this corresponds to assuming rigid motion of large crustal blocks. The second application (II) solves for the velocity gradient tensor only and thus ignores fault contributions to the relative motion field, i.e., assumes that all faults have been locked at the surface during the observation period. Finally, the third application (III) is the joint approach which solves for both fault slip and the velocity gradient field. We invert for all three model types and provide an analysis of the results for comparison.

[16] The density of our data set and our aim to model the regional deformation field restrict the estimation of the velocity gradient and fault slip to relatively substantial areas and fault segments, respectively. Around the LVF the station density allows a significantly denser parameterization compared to the rest of the model area. We include the surface traces of the six major geological faults [*Hu et al.*, 1996, 1997; *Yu et al.*, 1997] in our parameterization. The location of the fault traces have been digitized from *Yu et al.* [1997] to insure the station-to-fault relative positions. This approach leads to a total of 290 triangles, spanned by 192
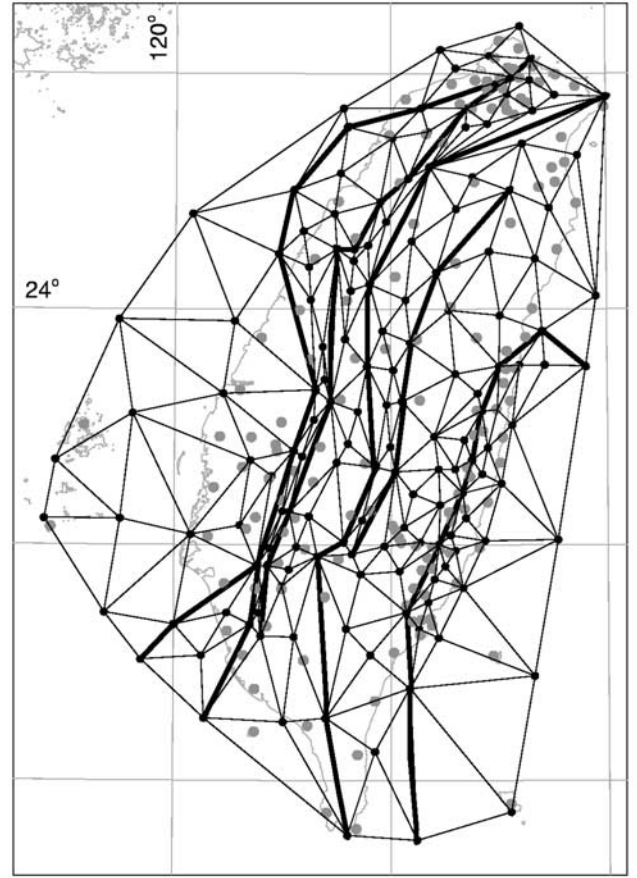

Figure 4. Final parameterization of the models of Taiwan. Thick lines indicate fault segmentation, solid dots are the triangle nodes, and grey dots are the site positions. Note that in our choice for the triangle nodes we are not restricted to the locations of the observation sites. Triangles do not intersect faults. Nodes at the fault are doubled to allow the velocity gradient field to be discontinuous across faults.

nodes and 57 fault segments with 57 slip vectors (Figure 4). Though fault slip parameter damping is possible, inversion I proved to be overdetermined with acceptable model covariance and required no damping. For inversions II and III we aim for a solution with minimal regularization, acceptable covariance and resolution and a $\chi^2 \sim 1.0$. However, a larger χ^2 (2.89 for our preferred model) and slightly reduced spatial resolution are accepted to avoid spurious values typical of an underdamped solution. Note that we implement the 1σ standard deviations in our inversion procedure. Utilizing a 3σ standard deviation would result in a χ^2 of 0.48. The first derivative regularization is allowed to vary spatially depending on the number of integration paths crossing each triangle (hit count of the triangle): Triangles with less hits than 1/12 of the maximum hit count obtain an increased regularization weight (α_{2a} and α_{2b}, respectively). The final tuning parameters obtained for both inversion II and III were $\alpha_r = 3.0 \times 10^5$ (or a standard deviation of $\sigma_r = 1.4 \times 10^{-6}$ Myr^{-1}) for the curl constraints and $\alpha_0 = 1.0 \times 10^8$ for the boundary damping, $\alpha_1 = 4.0 \times 10^7$ for the amplitude damping and, $\alpha_{2a} = 5.0 \times 10^{10}$ and $\alpha_{2b} = 2.0 \times 10^{11}$ for the spatially dependent first derivative operator on

Table 1. Aspects of the Inversion Parameterization and Average Results for Inversions I, II, and III[a]

i	T_n	T_t	K	χ^2	$\tilde{r}_m$	$\tilde{\sigma}_m^c$, 10^{-8} yr^{-1}	$\tilde{\sigma}_m^f$, mm yr^{-1}
I	-	-	114	24.4	1.0	-	0.13
II	155	290	-	4.96	0.65	1.25	-
III	192	290	114	2.89	0.62	1.46	0.22

[a]Key i, inversion; T_n, number of model nodes; T_t, number of triangles; K, number of fault segments; $\tilde{r}_m = 1/M \sum_{i=1}^{M} R_{ii}$, the average resolution, with R_{ii} the diagonal elements of the resolution matrix and M the number of model parameters; $\tilde{\sigma}_m^c = 1/M_c \sum_{i=1}^{M_c} \sqrt{C_{ii}}$, the average standard deviation for the components of $\nabla\mathbf{v}$, with $M_c = 4T_n$ the number of components of $\nabla\mathbf{v}$; $\tilde{\sigma}_m^f = 1/M_f \sum_{i=1}^{M_f} \sqrt{C_{ii}}$, the average standard deviation for the components of $\mathbf{f_k}$, with $M_f = 2K$ the number of slip components.

high hit count $\left(>\frac{1}{12}*\max\right)$ and low hit count $\left(<\frac{1}{12}*\max\right)$ regions, respectively. The fault slip vectors in inversions I and III were never subjected to damping. Table 1 provides an overview of some aspects of the inversion parameterization and average results for inversions I, II, and III.

5.1. Inversion I: Fault Slip Only

[17] In an attempt to fit the data by pure fault motion, i.e., assuming rigid crustal blocks, we only consider the six major geological faults on Taiwan. In the model the faults are represented by 57 slip rate vectors, each consisting of a fault normal and a fault parallel component, resulting in a total of 114 model parameters. The inverse problem proves to be overdetermined (perfect resolution), but the solution, with small model covariance, shows large data misfits which can not be accommodated by the 95% confidence error ellipses ($\chi^2 = 24.4$; Figure 5a). Using a more detailed fault parameterization of allowing twice the amount of slip model parameters per fault does not lead to a significant reduction of the data misfit nor renders a significantly different slip solution. A comparison with neotectonic observations of fault slip also fails the test. For instance, the solution for slip on the Longitudinal Valley fault comprises a combination of thrust and left-lateral motion, consistent with geological observations (Figure 5b). However, the magnitude of the slip is significantly larger than the observed slip rates determined from geological and creep meter measurements [*Angelier et al.*, 1997; *Lee et al.*, 2001]. The Lishan fault accommodates significant thrust movement on its northern segments, where geological evidence shows left-lateral movement in the north with increasing thrust movement toward the south [*Lee et al.*, 1997]. While the modeled left-lateral motion on the Chaochou-Chishan-Chuchin fault is supported by geological
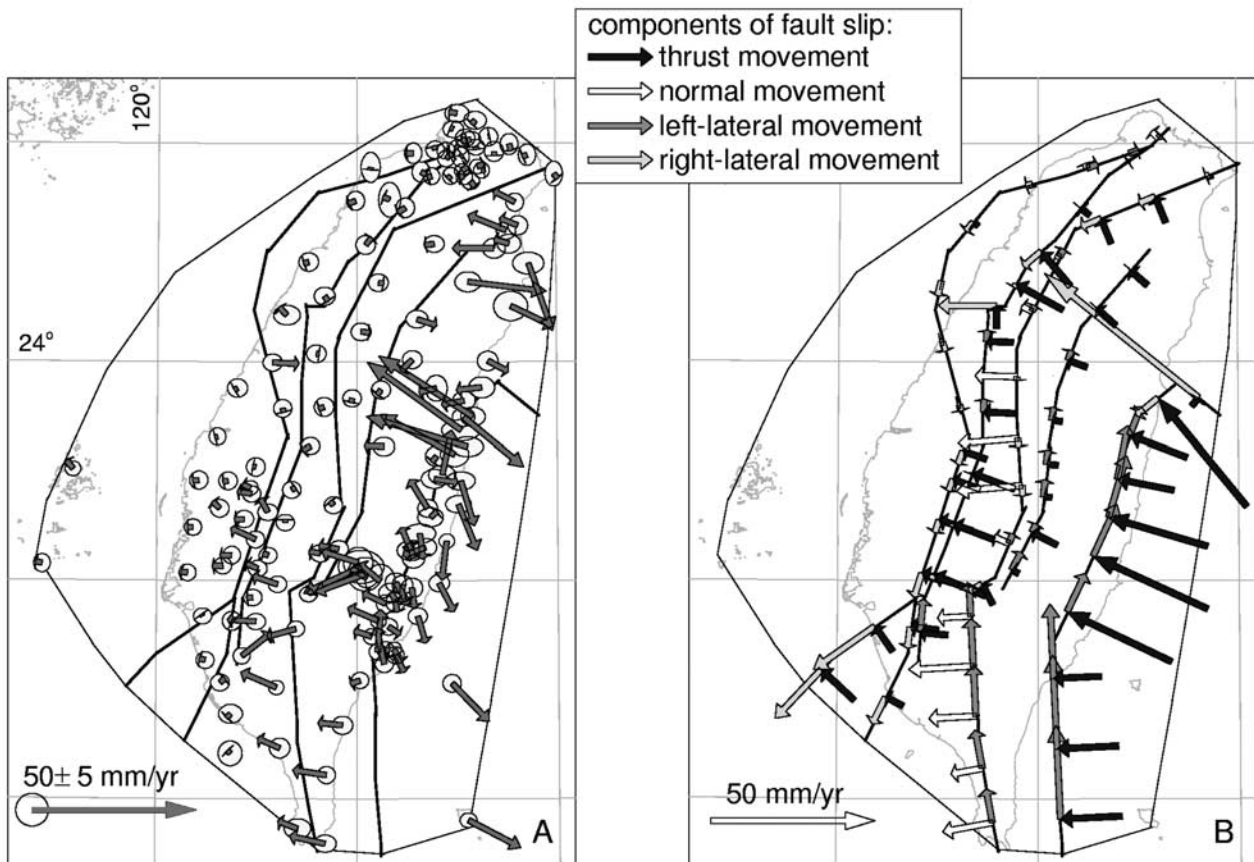

Figure 5. Solving for fault slip only. (a) Data misfits. Since our data are the relative velocities between every pair of stations, we determine the misfit at each station by taking the difference between the predicted velocity and the data velocity for each path connecting this station and determine the average. We compare it with the average error ellipse of the station, which is also determined from the error ellipses of all these paths. (b) Fault slip solution.
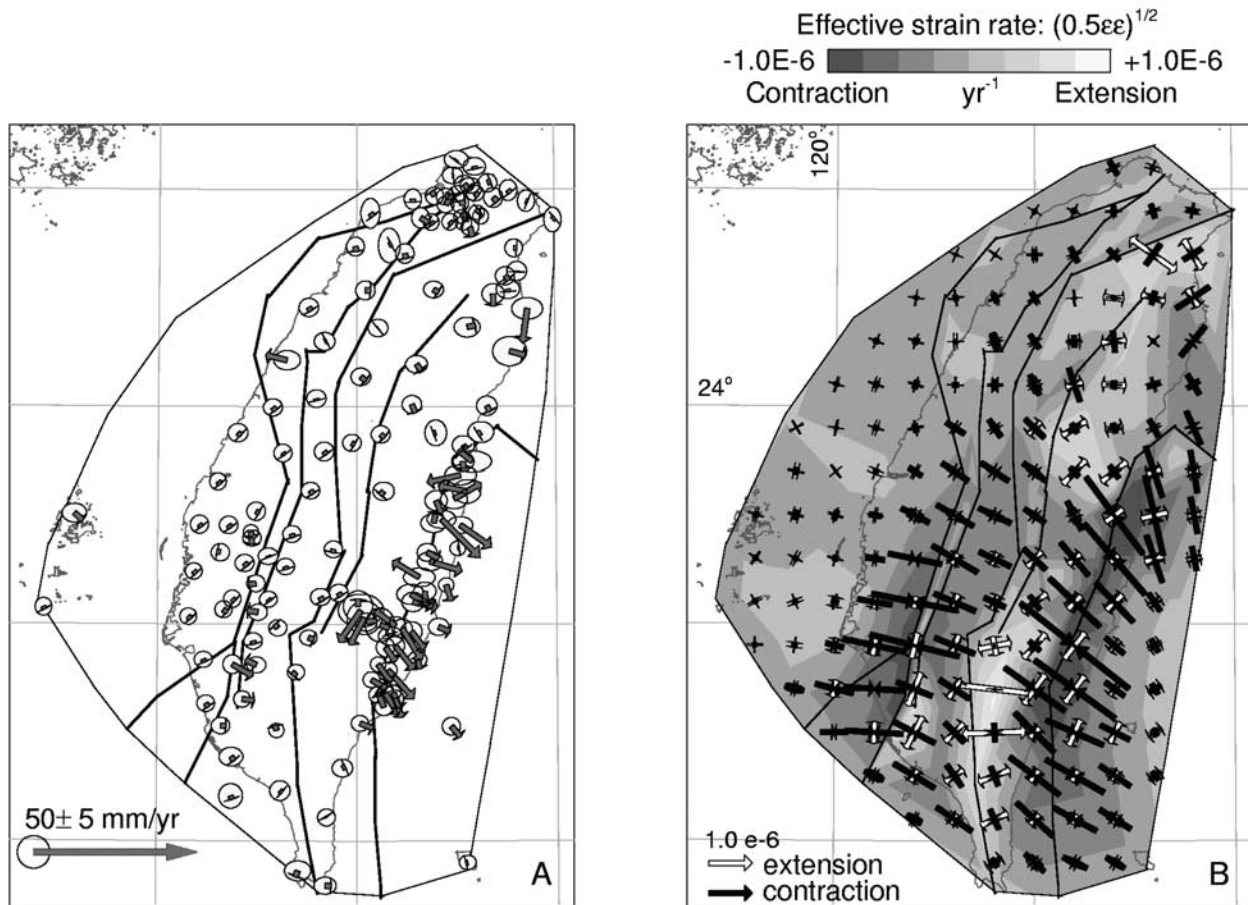
Figure 6. Solving for continuous deformation only. (a) Data misfits. (b) Strain rate field. The contouring denotes the effective strain rate ($=(1/2\epsilon_{ij}\epsilon_{ij})^{1/2}$). The arrows denote the principle strain rates: contraction (red) and extension (blue). See color version of this figure in the HTML.

observations, no evidence of the normal component has been found [*Lacombe et al.*, 2001]. The relative increase in thrust movement on the Chukou complies with geological observations [*Yu et al.*, 1997].

[18] Since we have only parameterized the six major active faults in the Taiwan region, we acknowledge the possibility of an improved data fit should minor fault systems be included. Here, we only test whether rigid motion of large crustal blocks (implicitly defined by adopting the major fault systems) can fit the data. In inversion III the minor faults and elastic loading are implicitly represented by the velocity gradient field. On account of the poor data fit and the poor comparison to neotectonic observations, we conclude that the hypothesis of pure rigid block motion cannot explain the GPS data.

5.2. Inversion II: Continuous Deformation Only

[19] In this application we do not solve for fault motion contributions to the velocity field. The parameterization consists of 290 triangles, spanned by 155 model nodes. Each node generates 4 components of the velocity gradient tensor, which results in a total of 620 model parameters. The data misfit ($\chi^2 = 4.96$; Figure 6b) is significantly better than obtained for model I. Largest misfits are found in the Longitudinal Valley region, where many GPS stations are

close to either side of the LVF (Figure 6b). From Figure 2 we infer that the GPS velocity changes strongly when crossing the fault as a result of fault motion not modeled in this inversion.

[20] Most of the convergence between the EUP and the PSP is absorbed in the Longitudinal Valley region. Extension is found in the southern Central Range (CR) and the Ilan Plain (IP). Large contraction can also be seen just east of the Deformation Front (Figure 6a). *Lee and Angelier* [1993] determined the strain rates for the central part of the Longitudinal Valley from trilateration data assuming that the crustal deformation should be modeled by continuous crustal flow. They show contraction rates at Juisui, Yuli, and Chihshang of (all expressed in yr^{-1}) 2.3×10^{-6}, 3.1×10^{-6}, and 2.1×10^{-6}, respectively, with a consistent N132°E trend. We find strain rates of $1.48 \pm 0.02 \times 10^{-6}$ in N140°E at Juisui, $0.86 \pm 0.02 \times 10^{-6}$ in N137°E at Yuli, and $1.35 \pm 0.02 \times 10^{-6}$ in N133°E at Chihshang, which are consistently smaller. This could be due to the differences in scale between their dense triangulation networks and our sparser GPS network and our coarser parameterization [*Kahle et al.*, 2000; *Nyst*, 2001]. *Yu and Chen* [1998] performed a study similar to that of *Lee and Angelier* [1993] for the southern part of the Chukou fault. They used the data of 5 years of GPS campaigns (1993–1997) to study spatial and temporal variations in crustal
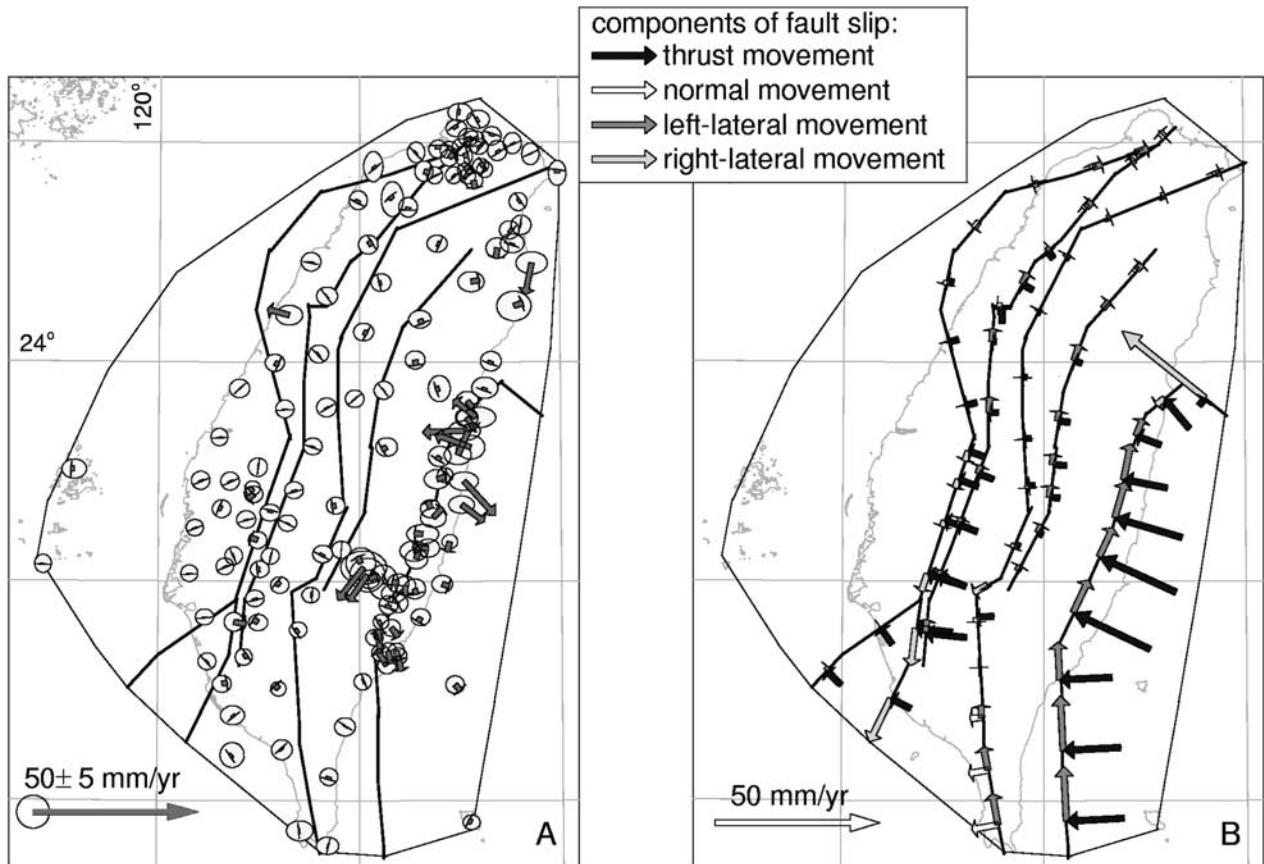
Figure 7. Joint solution. (a) Data misfits. (b) Fault slip solution. For further explanation, see Figure 6.

strain. Their calculated contraction rates of 0.48×10^{-6} yr^{-1} in N119°E at the central part of the Chukou fault increase to 2.01×10^{-6} yr^{-1} in N109°E farther to the south. Here we find an increase from $0.47 \pm 0.02 \times 10^{-6}$ yr^{-1} in N119°E to $1.08 \pm 0.02 \times 10^{-6}$ yr^{-1} in N96°E. They also determined extension rates in the south of 0.7×10^{-6} yr^{-1} in N18°E. This agrees reasonably well with our extension rates of $0.50 \pm 0.02 \times 10^{-6}$ yr^{-1} in N27°E in the same area.

[21] Though this application clearly offers a better data fit than the inversion for fault slip only (I), it remains inconsistent with neotectonic observations. Further, the presence of major, active faults in this region is undisputed.

5.3. Inversion III: Fault Slip and Continuous Deformation

[22] The joint inversion utilizes the same triangular grid as inversion II. On the fault traces duplicate model nodes are used to allow decoupling across the fault. The joint inversion is thus based on the same 290 triangles spanned by 192 model nodes and an additional 57 slip vectors, yielding a total of 882 (768 for $\nabla \mathbf{v}$ and 114 for $\mathbf{f}_k$) model parameters. Some of the data misfits for this joint inversion are slightly larger than the average 95% confidence ellipses leading to an average data misfit χ^2 of 2.89 (Figure 7a). We observe that the few misfit vectors that exceed the limits of the data confidence ellipses are still primarily located in the Longitudinal Valley region, where deformation is strongest. Comparison with the data (Figure 2) shows that the misfit vectors denote local differences within the trend of the data.

Our adopted parameterization is too coarse to model these strong local variations in relative motion. Before analyzing the fault slip (Figure 7b) and the strain and rotation rate fields (Figures 8a and 8b) we will discuss the covariance and resolution of the solution.

5.3.1. Covariance and Resolution

[23] From the model covariance matrix C we extract the standard deviations in the estimates of our model parameters $\left(\sigma_i = \sqrt{C_{ii}}\right)$. For the velocity gradient field we plot the σ_i corresponding to a 95% confidence level as two contour plots: one for the ϕ derivatives (longitude) (Figure 9a) and one for the θ derivatives (latitude) (Figure 9b). The larger errors ($\sim5 \times 10^{-8}$ yr^{-1}) occur along the southwestern extent of the Deformation Front and in the north-northwestern region of the model area. In regions with a small amplitude ($\sim1 \times 10^{-8}$ yr^{-1}) the solution becomes insignificant. The errors of the fault slip parameters, plotted as 95% confidence error vectors in the θ and ϕ direction (Figure 9c), are a factor 10 smaller than the average magnitude of fault slip obtained in the solution.

[24] Figures 9d and 9e show contour plots for the diagonal elements of the resolution kernel of the velocity gradient field. The interior of the study region is relatively well resolved with diagonal elements exceeding 0.75. The difference between resolution in latitude and longitude can be understood by realizing that due to the better N-S spread of observations (compared to E-W) latitudinal variations are better resolved. Reduced resolution at the boundary of our modeling area is due to the influence of the regularization.
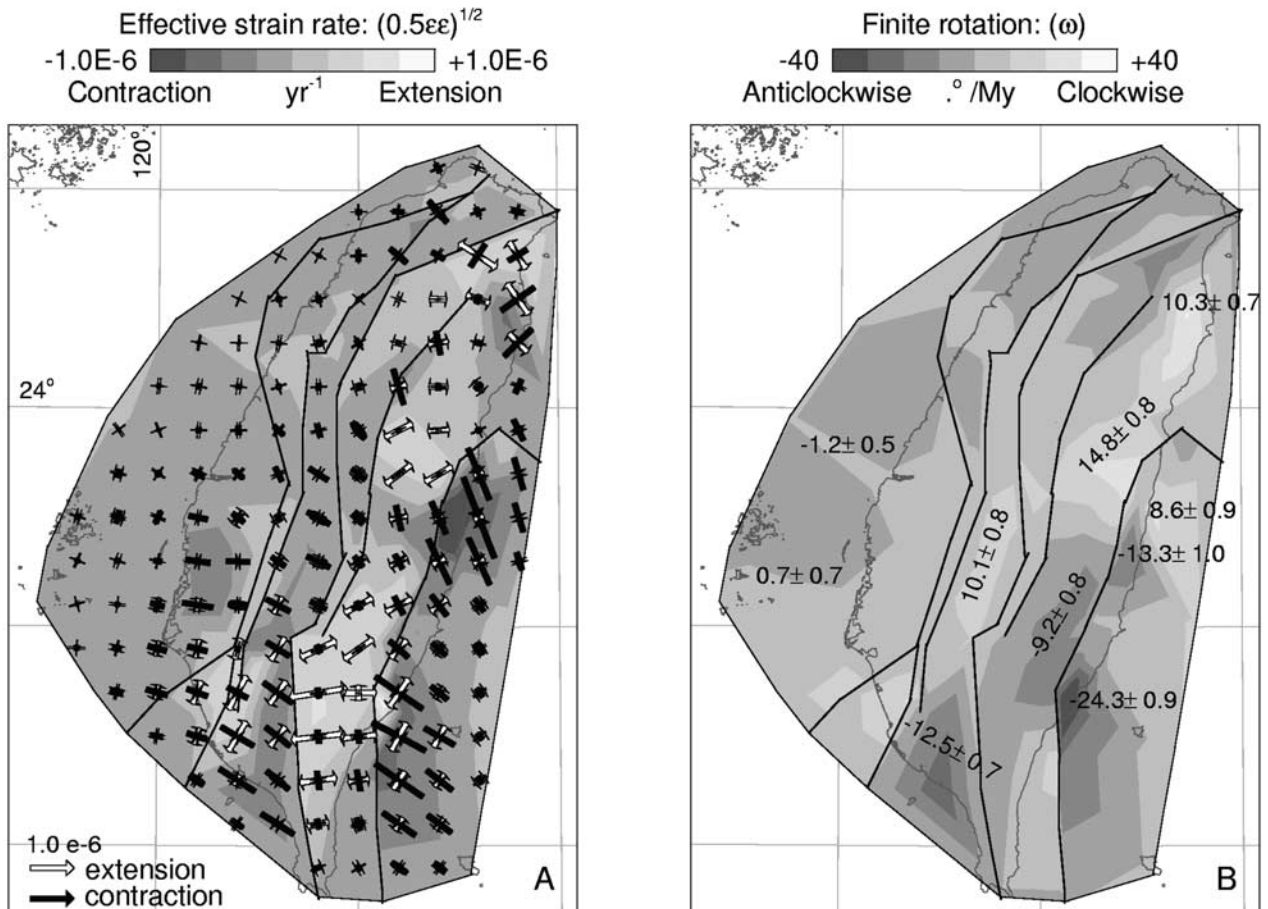
Figure 8. Joint solution. (a) Strain rate field. (b) Rotation rate field in degrees per million years. The numbers refer to local averages of relatively strong rotation rates and their 1σ errors. See color version of this figure in the HTML.

The reduced resolution offshore Taiwan in the northwestern part of our modeling area can be attributed to the poor data coverage in this part of the model. In the interior of the model the resolution is reduced due to a trade-off between fault slip and the velocity gradient This can be observed between the Deformation Front and the Chukou fault, around 24°N between the Chukou fault and the Chaochou-Chishan fault, and between the Chaochou-Chishan fault and southern Lishan fault. We note that the fault slip thus modeled may represent a combination of fault creep and interseismic signal, depending on the trade-off between the velocity gradient field and fault motion. This trade-off occurs in case of lack of data to couple fault motion to the velocity gradient field in a kinematic inversion [*Nyst*, 2001; *Spakman and Nyst*, 2002]. The trade-off is best resolved in areas with relative motion observations close to the fault zones. In areas where this is not the case, interseismic signal due to block motion may be introduced in the slip solution, while the fault may be locked. This trade-off also affects the amplitude of the velocity gradient estimate in the proximity of the fault. We note that a solution for only continuous deformation (solution II of this study) implicitly reflects pure elastic loading of locked faults. We further note that the trade-off problem is not a feature of the *Spakman and Nyst* [2002] method, but is a problem for any interpretation method of relative motion data. We refer to *Spakman and Nyst* [2002] for a further discussion on this topic.

5.3.2. Fault Slip Contribution

[25] In the joint solution we find significantly reduced fault slip rates compared to inversion I, though the sense of motion is reasonably consistent between the two solutions. The fault slip contribution of the joint solution (Figure 7b) shows relatively small horizontal slip of the order of ~2 mm yr^{-1} on most fault segments. Larger horizontal slip rates are observed on the southern segments of the Chukou fault and on the Longitudinal Valley fault. Large vertical rates have been determined on Taiwan [*Lin*, 1998; *Yu and Kuo*, 2001] but are not reproduced by our model since we only consider horizontal velocities/rates. Slip rates on the Longitudinal Valley fault vary from ~19 mm yr^{-1} with an azimuth of N124°E at Taitung to 25 mm yr^{-1} in N136°E at Yuli and 7.8 mm yr^{-1} in N151°E at Hualien. *Yu et al.* [1990] showed that the Longitudinal Valley fault is a very weakly locked or almost freely creeping fault. At Tapo, *Angelier et al.* [1997] determined present-day rates based on detailed surveys of faulted concrete structures. Their rate of 22 mm yr^{-1} in N143°E compares reasonably with our value of 26.84 ± 0.22 mm yr^{-1} in N136°E. The difference might be explained by the scale differences of the very local observations and our more regional parameterization.
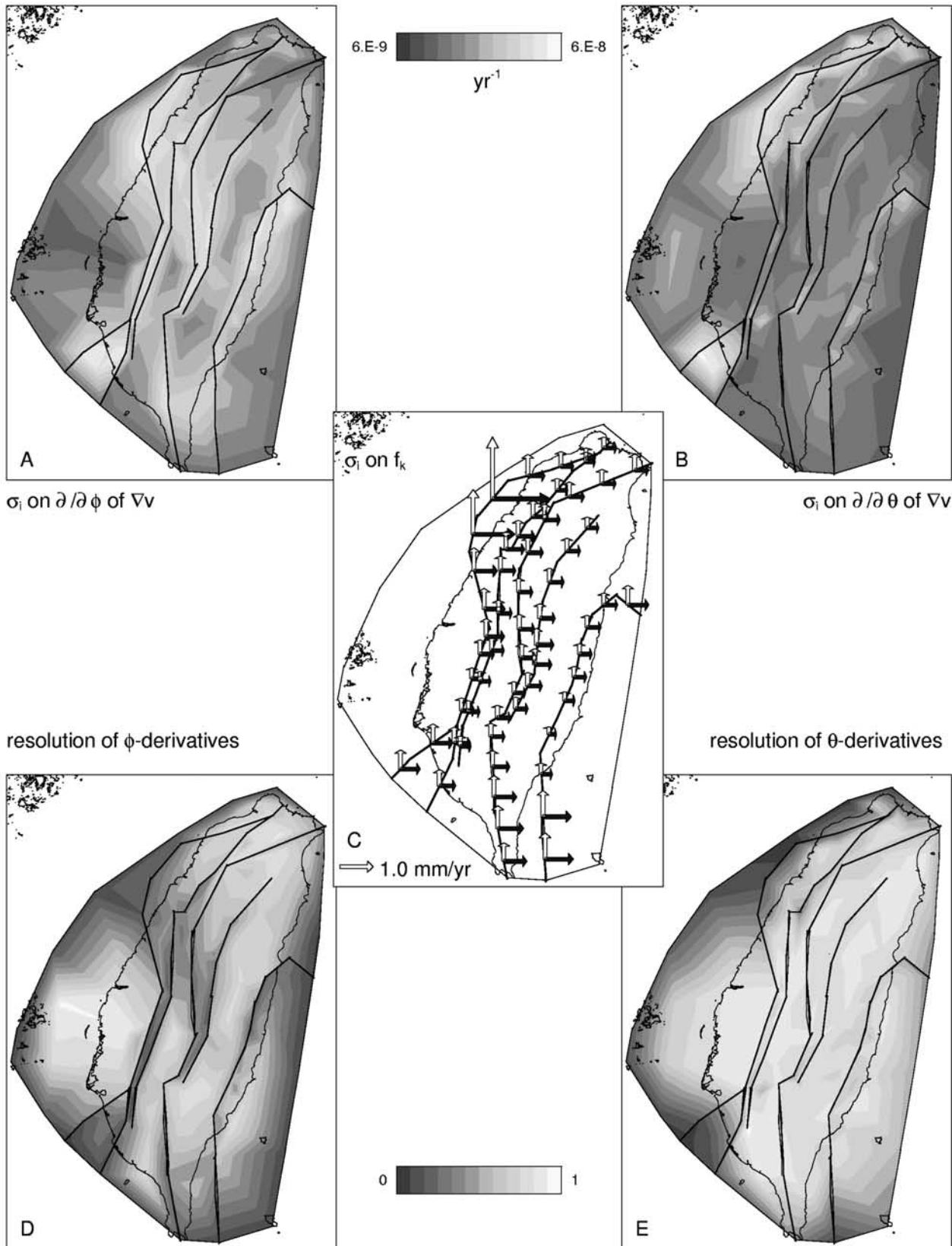
Figure 9. Covariance and resolution of the joint inversion solution. The covariance is represented as the model standard deviations $\left(\sigma_m = \sqrt{C_{ii}}\right)$. (a) Contour plot of the 95% confidence σ_i on ∇v_θ, (b) contour plot of the 95% confidence σ_i on ∇v_ϕ, (c) 95% confidence σ_i on $\mathbf{f}_k$ plotted as error vectors in the θ direction and ϕ direction, (d) contour plot of the resolution of ∇v_θ, and (e) contour plot of the resolution of ∇v_ϕ.

[26] The Lishan fault shows left-lateral movement at the northern segment changing to thrust movement more to the south. This variation in movement is in agreement with geological observations done by *Lee et al.* [1997]. *Yu et al.* [1997] found a significant increase in shortening rates toward the south along the Chukou fault, which is in support of the increase of thrust movement we observe in our model. We further find that the Deformation Front acts as a right-lateral thrust, which is consistent with the observations of *Lacombe et al.* [2001].

5.3.3. Strain Rate Contribution

[27] The parameterization of faults in application III allows the velocity gradient field to be discontinuous across active faults. The implementation of the faults significantly reduces the magnitudes of the strain and rotation rates compared to application II, especially around the Longitudinal Valley fault and the Chukou fault. The magnitudes obtained for the strain rate field still remain amongst the largest estimates on Earth for interseismic deformation.

[28] The strain rate field (Figure 8a) shows a general behavior of NW-SE contraction in the Longitudinal Valley of eastern Taiwan. In southwestern Taiwan we observe an anticlockwise rotation of the principle axis direction to E-W contraction. The Peikang High is found to have relatively small strain rates. Comparing this trend with the stress field modeling results of *Hu et al.* [1996] we find a general agreement. However, differences between their results and our solution are observed, especially around the IP. This may be due to ignoring the opening of the Okinawa Trough (OT) in their elastic-plastic model, which could have a significant effect on the strain rates in northeastern Taiwan. Another cause for discrepancies can be that stress and strain directions do not necessarily align in case of elastic-plastic rheology, which hampers a comparison between their stress directions and our strain directions. The magnitude of the strain rate field decreases toward the north.

[29] East of the Longitudinal Valley fault, relatively large NW-SE contraction dominates the deformation. In contrast, the central and southern CR show a dominant NE-SW to E-W extension. Geologically, this extension is inferred from normal faulting in the orogen [*Crespi et al.*, 1996; *Kosuga et al.*, 1988], thermal observations [*Crespi et al.*, 1990] and normal fault type earthquake swarms [*Lin and Tsai*, 1981; *Rau*, 1996]. The Western Foothills (WF) are subjected to a WNW-ESE contraction accompanied by a significantly southward increasing NNE-SSW extension. This trend is in agreement with Pleistocene paleostress patterns in southwestern Taiwan [*Lacombe et al.*, 1999; *Rocher et al.*, 1996]. In the IP we find profound NW-SE extension, which concurs with the inferred extensional direction in the Okinawa Trough [*Herman et al.*, 1978; *Kimura*, 1985; *Sibuet et al.*, 1987].

5.3.4. Rotation Rate Contribution

[30] The rotation rate tensor is given by the antisymmetric part of the velocity gradient tensor (Figure 8b). Strictly speaking, the obtained relative rotation rates apply to rigid rotations of small equidimensional blocks. Interpretation of regional (anti) clockwise rotations can be made if on average the obtained rotation rates are (negative) positive. Since we are not able to solve for a net uniform rotation of the entire study region a comparison with paleomagnetic

block rotations is not straightforward. This is further complicated by the fact that almost all paleomagnetic observations are older than 8 Ma [*Lee*, 1993; *Miki et al.*, 1993] and hence occurred prior to the last collisional phase [*Ho*, 1988; *Kao et al.*, 1998; *Teng*, 1990]. We notice that many large regions with the same sense of rotation rate are bounded by the faults which is indicative of fault motion.

[31] Model III (Figure 8b) shows two regions with large anticlockwise rotation rates in the CoR, where, just offshore the northern section of the CoR, equally large clockwise rotations are obtained. This offshore area and the area around Taitung are, however, poorly resolved and care should be taken when interpreting these rotation rates.

[32] The WF are divided in three blocks with opposing rotations; Northern Taiwan is dominated by anticlockwise rotations, the central part experiences clockwise rotation averaging $10.1 \pm 0.8° \text{ Myr}^{-1}$ as the southern WF are subjected to $12.5 \pm 0.7° \text{ Myr}^{-1}$ of anticlockwise rotation on average. The CR shows a similar division: The northern section undergoes averagely $14.8 \pm 0.8° \text{ Myr}^{-1}$ of clockwise rotation, the middle section is subjected to anticlockwise rotation averaging $9.2 \pm 0.8° \text{ Myr}^{-1}$, and the southern section shows reduced anticlockwise rotation in the west and clockwise rotation in the east. The intersections of the oppositely rotating blocks coincide with the two major transfer fault zones on Taiwan. Only the southern region of the Coastal Plain undergoes a clockwise rotation of a few degrees per million years. The Ilan Plain is rotating clockwise with a rate of $10.3 \pm 0.7° \text{ Myr}^{-1}$ on average.

5.3.5. Comparison to Lithospheric Stress Data

[33] We compare the principle axes of our strain rate field with the principle stress axes from earthquake focal mechanisms. Since we only model the two-dimensional horizontal strain rate tensor, we compare it to the horizontal components of the seismic moment tensor. These four components were extracted from the Harvard moment tensor solution of each earthquake within the modeling area with magnitude larger than 4 and depth less than 50 km. In our comparison we make a distinction between shallow events (<20 km) and the deeper events. Though we are aware that the deeper seismicity may be related to lithospheric deformation (subducting slab), we include the deeper events to allow for comparison with events in the crustal root of the orogen underneath the Central Range. The principle axes of seismic moment tensors do not need to coincide with those of the surface strain rates since (1) the seismic moment tensors reflect local release of stress (which not necessarily coincides with regional strain rate directions) and (2) the surface strain rates do not necessarily reflect deformation at depth.

[34] In the Western Foothills we find a reasonable agreement in the directions of the principle axes for all events. In all other areas a consistent misfit exists for both shallow and deep events. In the southern Central Range the E-W compression at depth is in complete contrast to the E-W extension of our model. We believe that these disagreements should be attributed mostly to the fact that those surface velocities which are the response to deeper crustal processes not necessarily contain all information on the deformation occurring in the deeper crust. Therefore a combination with crustal deformation data (e.g., seismicity)

is useful to study crustal processes driving the surface deformation.

6. Geometry of the Subduction System

[35] Of basic importance for understanding the determined strain and rotation rates and fault slip is the geometry of the two subduction systems in the mantle. Numerical modeling predicts that subduction of an continent-ocean boundary (COB) leads to favorable conditions for detachment of the oceanic lithosphere [*Van de Zedde and Wortel*, 2001; *Wong A Ton and Wortel*, 1997]. Several recent studies have adopted the hypothesis of detachment of the EUP slab under northern and central Taiwan in order to explain the ongoing subduction of the PSP slab [*Lallemand et al.*, 1997, 2001; *Teng et al.*, 2000]. Analogue models [*Chemenda et al.*, 2001] demonstrate the possible conjunction of EUP slab detachment and incipient westward subduction of the PSP under Taiwan.

[36] The question remains whether slab detachment is actually occurring. *Lallemand et al.* [2001] base their interpretation of slab detachment on the global tomographic mantle model of *Bijwaard et al.* [1998], which shows predominantly low *P* wave speeds in the upper 100 km of the EUP subduction. However, since the nonsubducted part of the Chinese continental lithosphere is imaged with similar low wave speeds, it is difficult to discriminate between a detached slab and subducted continental lithosphere particularly in the upper 100–150 km of the mantle. Below this depth range the EUP slab is visible in the mantle tomography. *Teng et al.* [2000] invoke slab detachment as the driving force behind the high uplift rates and large heat flow observed in the eastern Central Range. The maximum uplift rates and largest heat flows are currently observed between 23°N and 23.5°N, which would suggest that the tip of the southward propagating detachment tear has advanced significantly south of this location [*Wortel and Spakman*, 1992, 2000]. However, both seismicity and seismic tomography (Figure 10) contradict this suggestion by showing a continuous slab up to 23°N.

[37] The assumption of slab detachment is required if the northward extension of the EUP slab beneath Taiwan intersects with the PSP slab. Figure 10 shows cuts from the tomographic model of *Bijwaard and Spakman* [2000], which differs from earlier work [*Bijwaard et al.*, 1998] as a result of 3-D ray tracing to correct for seismic ray bending effects caused by the 3-D velocity structure of the mantle. For the Taiwan region this leads to an improved definition of the slab geometry. The relatively fast (blue) anomalies north of 24°N and east of 122°E image the north-north-westward plunging PSP subduction zone along the Ryukyu trench. Similarly, the eastward dipping EUP is visible south of 24°N and at longitudes centered around 122°E. For depths above 145 km the EUP slab is best delineated by intermediate seismicity. Below this depth the slab reaches 24°N at most (the latitude of Hualien). We assume that the PSP slab and the EUP slab are at the point of making contact with each other at Hualien. On account of these images, slab detachment of the EUP below north to central Taiwan does not at present seem a strong requirement to create space for the PSP to subduct in a northwestward direction. The image associated with the EUP slab does not

show significant lateral displacement with depth, which attests of its steep dip. This could be attributed to resistance of the Chinese continental margin to engage in the westward roll-back of the EUP slab (viewed in a Eurasian fixed reference frame).

7. Model Interpretation
7.1. Southern Taiwan: Southward Extrusion

[38] In southern Taiwan our surface deformation model exhibits strain rates of almost pure E-W contraction, which is consistent with ongoing collisional shortening in the orogen. The contractional rates are accompanied by southward increasing, predominantly N-S oriented extensional strain rates (Figure 8a). We find right-lateral thrust motion of $\sim$14 mm yr^{-1} in a N54°W direction on the Deformation Front and left-lateral normal motion of 6–13 mm yr^{-1} in direction N110°–130°E (increasing southward) on the Chaochou-Chishan fault (Figure 7b). The block bounded by these faults is subjected to an anticlockwise rotation rate of $\sim$12.5° Myr^{-1}, where the areas on either side of this block are experiencing clockwise rotation rates or significantly smaller anticlockwise rotation rates (southern Central Range; Figure 8b). These patterns of surface deformation are indicative of lateral extrusion toward the Manila accretionary wedge south of Taiwan. To the north the extrusion is terminated by the Chishan Transfer Fault Zone (Figure 11). The analogue models of *Lu and Malavieille* [1994] also suggest a southward lateral extrusion of the sedimentary cover of the southern Western Foothills in response to the oblique collision between the PSP and the EUP. The southern Taiwan area is further characterized by low shallow seismicity with a significant increase at the base of the crust (Figure 12, cross-section A), and the results of geodetic retriangulation within the orogen [*Chen*, 1984] demonstrate that in this area subsidence prevails. These observations are in support of our interpretation of our surface deformation model in southern Taiwan.

7.2. Central Taiwan: Oblique Collision, Shortening, and Exhumation

[39] In the central section of the Western Foothills and western Central Range (Figure 1) the model surface strain rate field is dominated by WNW-ESE contraction and clockwise rates of $\sim$10.1° Myr^{-1} (Figures 8a and 8b). We obtain right-lateral motion with an increasing thrust component for the Deformation Front, left-lateral thrust motion on the Chukou fault, insignificant motion on the Chaochou-Chishan fault and minor left-lateral thrust motion on the Lishan fault (Figure 7b). These modeling results represent the surface response to the ongoing oblique collision causing shortening and shearing in the orogen. However, in the eastern Central Range (Figure 1) we obtain a dominant extensional principle strain rate. The principle direction of the extension rotates from NE-SW in the central northern eastern Central Range to E-W in the south, in agreement with geological observations gathered in the area [*Crespi et al.*, 1996; *Lu et al.*, 1998]. The extension is accompanied by an anticlockwise rotation rate of $\sim$9.2° Myr^{-1}. Recent reports of leveling measurements across the Central Range describe uplift rates as high as 36–42 mm yr^{-1} for the past decade [*Liu*, 1995a] especially
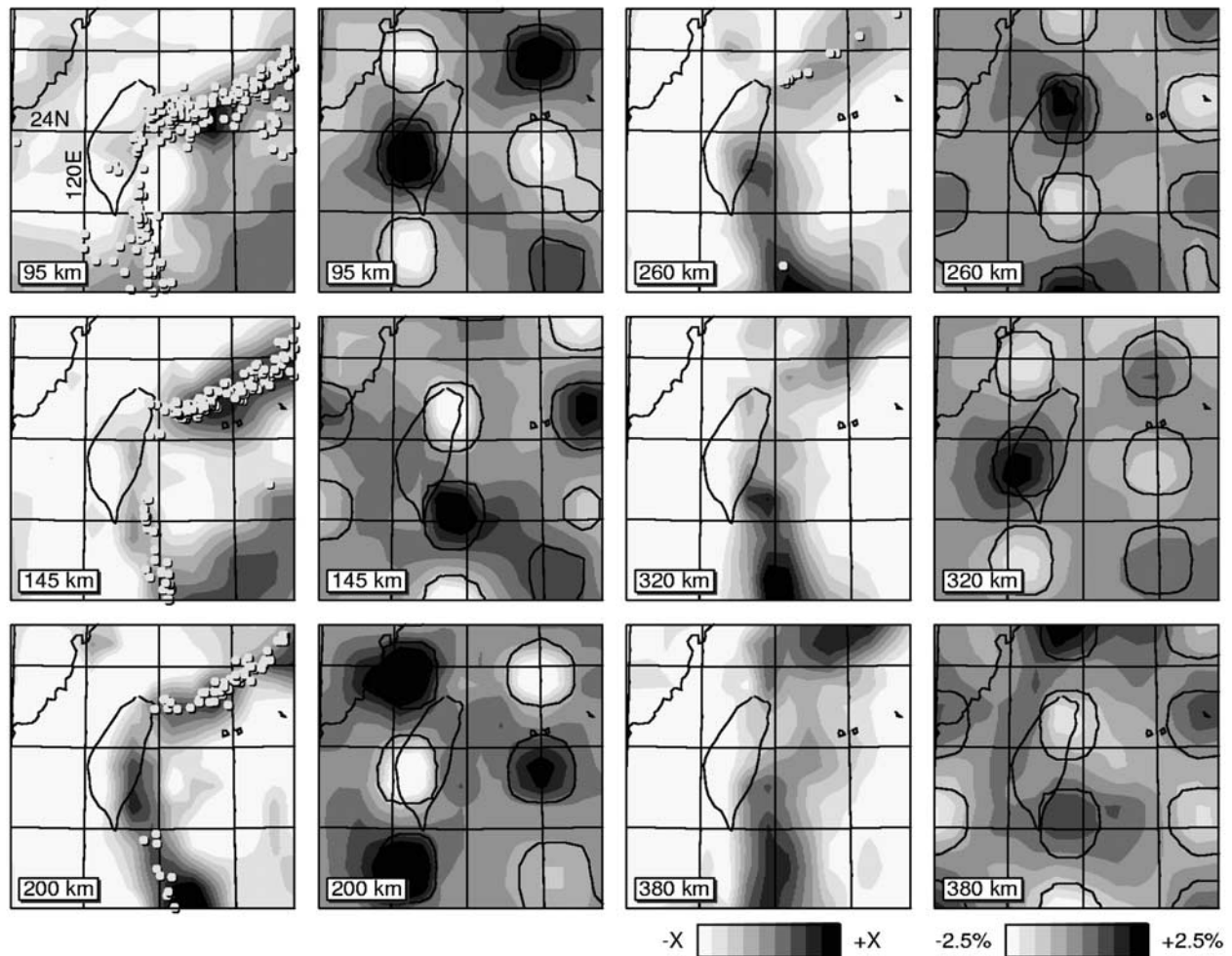
Figure 10. Layer cuts from the global tomographic mantle model of *Bijwaard and Spakman* [2000]. (left) *P* wave velocity anomalies between 95 and 380 km (depths indicated) in percentages of the following reference velocities (from top to bottom) 8.047, 8.119, 8.275, 8.482, 8.701, and 8.913 km s^{-1}. White dots denote intermediate depth hypocenters within 25 km of each layer depth. The grid of black lines is longitude and latitude lines in steps of 2 degrees (see top left panel for 2 values). (right) Results of a sensitivity test for estimates of spatial resolution in which the image recovery is tested of a synthetic velocity model consisting of isolated blocks (circular outlines) of 1.2° in size and a thickness of about 50 km. The amplitudes are of alternating sign and the blocks are shifted in depth. The colors denote the recovery of the synthetic model. Mild smearing effects between the synthetic blocks are visible at all depths, but the synthetic blocks are generally well recoverable, particularly in the upper 200 km under Taiwan. Below this depth, resolution reduces gradually. We conclude from this (and other sensitivity tests) that the tomographic image of the actual Earth (left) is interpretable at length scales of 50–60 km. See color version of this figure in the HTML.

between 23°N and 23.5°N [*Kosuga et al.*, 1988]. A feasible explanation of our surface deformation patterns, the high uplift rates, and the high-grade metamorphic core complexes observed in the eastern Central Range (section 2) could be the exhumation of crustal material. Regional tomography of *Rau and Wu* [1995] (Figure 13) shows a thickening of the crust under the high elevations of the Central Range, where the deepest part is offset to the east. In the north the low-velocity root extends down to a depth of 35 km (v_p = 6.0 km s^{-1}). This is in agreement with a Moho depth of 33 km inferred from gravity Bouguer anomaly modeling [*Yen et al.*, 1998]. In both tomographic cross sections the velocity in the top 15 km under the Central Range is relatively high compared to the velocities underneath the Western Foothills and the Coastal Range. This coincides with a zone of relatively little seismicity found underneath the eastern Central Range (Figure 12). *Chemenda et al.* [2001], *Lin* [1998], and *Lin et al.* [1998] propose a model of crustal subduction followed by exhumation in a orogen normal direction of the eastern Central Range to account for the observations. In this model the continental crust of the South China Sea is subducted to midcrustal levels where it becomes detached from the mantle part of the lithosphere and exhumes. However, in this model
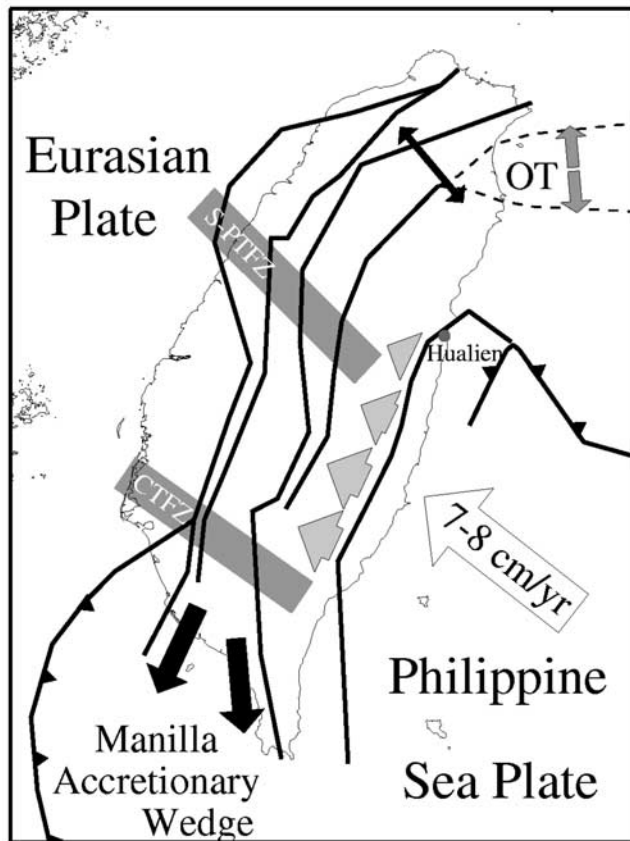
Figure 11. Schematic representation of the tectonic interpretations made in this study. Gravitational collapse (thin solid arrows) and opening of the Okinawa Trough (dark grey arrows) in northern Taiwan, ongoing collision with crustal failure, accretion and exhumation of crust in the Central Range of the central block (light grey arrows), lateral extrusion of the sedimentary cover to the Manila accretionary wedge in southwest Taiwan (wide solid arrows), and the development of a tear fault with incipient northwestward subduction at the transition between the two trench systems at Hualien. OT denotes Okinawa Trough.

the obliquity and southward propagation of the collision is not taken into account. Since collision commenced in the north and is progressively moving southward, the subducting continental crust in the north would reach critical conditions needed for its detachment from the mantle part well before its southern equivalent. Therefore it is reasonable to assume a southward propagation of the exhumation in conjunction with the collision (Figure 11). This southward propagation of the exhumation may cause the anticlockwise rotation observed in the eastern Central Range as well as deviate the principle directions of the extension to a more NE-SW orientation in the regions with maximum exhumation.

7.3. Northern Taiwan: Crustal Extension and Orogenic Collapse

[40] Most of northern Taiwan (north of the Sanyi-Pakua Transfer fault zone) is subjected to relatively small anticlockwise rotation rates ($0°-5°$ Myr^{-1}; Figure 8b) and left-lateral fault slip (Figure 7b). Strong clockwise rotation rates

of $\sim10.0°$ Myr^{-1} are found in the Ilan Plain. The strain rate field is characterized by relatively small NW-SE contraction corresponding to geological observations in the area [*Crespi et al.*, 1996; *Teng*, 1996]. On the basis of our model and the geological observations, the northern extent of the mountain belt is no longer subjected to active crustal shortening. However, the extensional regime due to the opening of the Okinawa Trough [*Liu*, 1995b; *Yeh et al.*, 1989] induces crustal stretching and gravitational collapse.

[41] The back arc extension in the trough is related to the southwestward migration and rotation of the Ryukyu trench [*Liu*, 1995b; *Yeh et al.*, 1989], which commenced 2 Myr ago [*Lee et al.*, 1991; *Lee*, 1993; *Miki et al.*, 1993]. The significant NW-SE extension obtained in our model in the Ilan Plain clearly portrays the on-land extension of the Okinawa Trough (Figure 11). Shallow seismicity in northern Taiwan is low, whereas the Ilan Plain is characterized by high, very localized shallow seismicity and an increased heat flow, which would be expected in a back arc basin. Thus the Okinawa Trough has acquired the ability to propagate into Taiwan along a preexisting weak zone, the Lishan fault. In the northern eastern Central Range the WNW-ESE extension may be due to a combination of the gravitational collapse and the crustal exhumation, as identified in the central and southern eastern Central Range (Figure 11).

7.4. The Coastal Range: Incipient Northwestward Subduction of the PSP

[42] In the Coastal Range, the modeled creep motion on the Longitudinal Valley fault reduces significantly northward from ~19 mm yr^{-1} with an azimuth of N124°E at Taitung to ~7.9 mm yr^{-1} in N151°E at Hualien (Figure 7b). Our strain rate field shows strong NE-SW contraction accompanied by large anticlockwise rotation rates in the Coastal Range and comparable clockwise rotation rates just offshore between 23.5°N and 24°N (Figures 8a and 8b). South of 23.5°N the NE-SW contraction is more moderate (though significant) and smooth and predominantly anticlockwise rotation rates are obtained. Some care should be taken when interpreting these results due to poorer resolution in this area especially in the φ derivatives. However, on the basis of the decrease in modeled fault motion significant contractional strain rates or a significant decrease in PSP motion are to be expected. Since there are no indications to suspect a change in PSP velocity at 23.5°N, 40–50 mm yr^{-1} of PSP motion has to be accommodated east of the Coastal Range. The focal mechanisms of the earthquakes in this region denote a fault with an average strike of 23°N and an average dip of 75° located just offshore the island of Taiwan (Figure 14). At Hualien (23.9°N), we plotted the seismicity along a profile striking perpendicular to this fault (Figure 12, cross-section D). The profile shows deep (up to 50 km), localized seismicity around the fault and indicates a northwestward dipping Wadati-Benioff zone. Seismically, the slab extends to approximately 75 km. The fault location is also tied with a significant gravity low observed in Hualien Canyon [*Yen et al.*, 1998]. Further, regional tomography [*Rau and Wu*, 1995] (Figure 13) shows a well-defined high-velocity zone ($v_p > 8.0$ km s^{-1}) underneath the Coastal Range and Central Range, which compares in size to the Wadati-Benioff zone of the PSP at the Ryukyu trench. On the basis of analogue modeling, *Chemenda et al.* [1997, 2001]
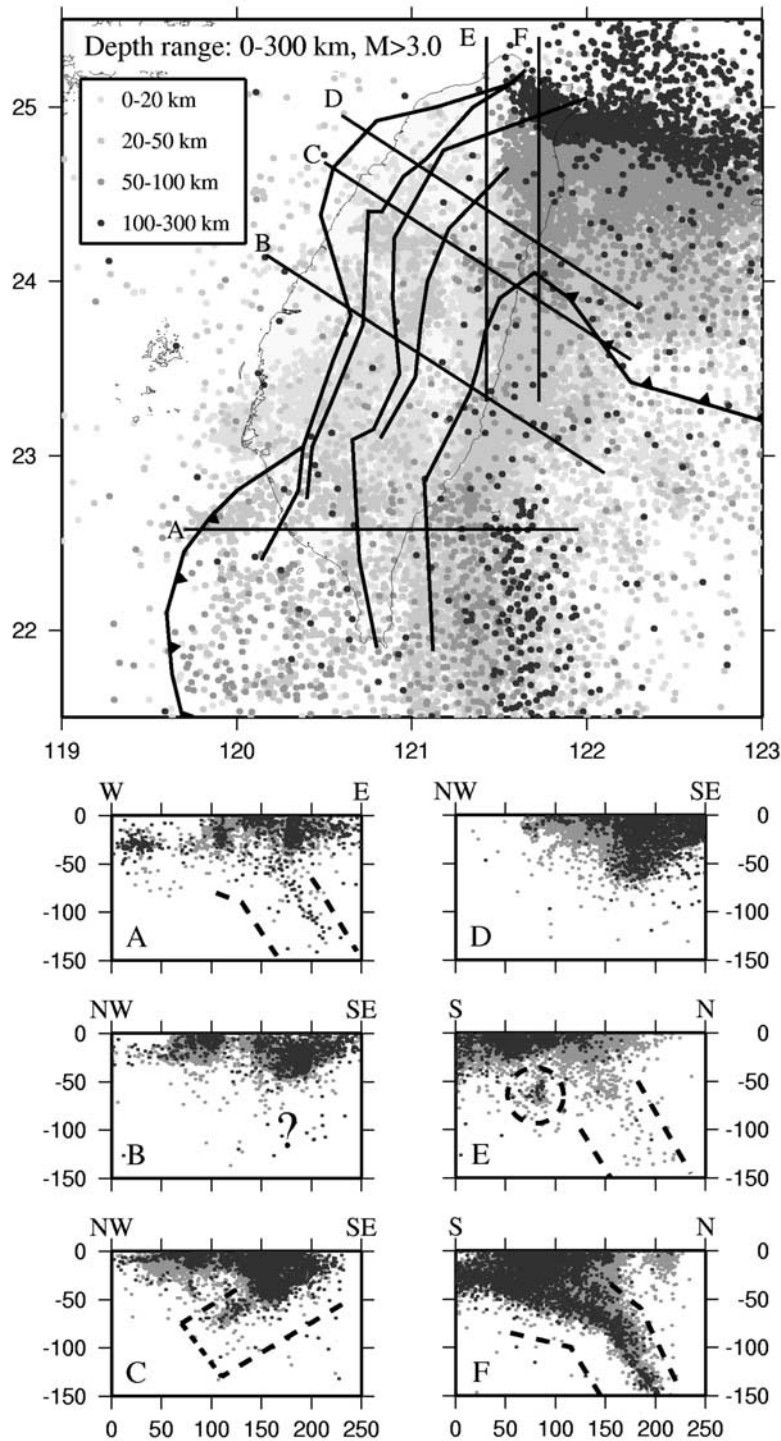
Figure 12. Local seismicity as cataloged by the Central Weather Bureau of Taiwan, between May 1900 and October 2000. Light grey dots in cross sections indicate 0 M 3. Solid dots in cross sections indicate $M > 3$. Events contained in dashed circle correspond to the incipient subduction outlined in section C.

propose the possible occurrence of incipient subduction of the PSP at the latitude of Hualien. Such incipient subduction would accommodate most of the convergence between the PSP and Eurasia. The hypothesis explains our surface deformation model and is in fact confirmed by the seismicity data and the regional tomographic model (Figure 11). The fault indicated by the focal mechanisms of events in

the area could represent the top of the PSP slab developing northwestward subduction below eastern Taiwan.

8. Geodynamic Evolution

[43] To provide an understanding for the present-day tectonic setting of Taiwan we consider the geodynamic
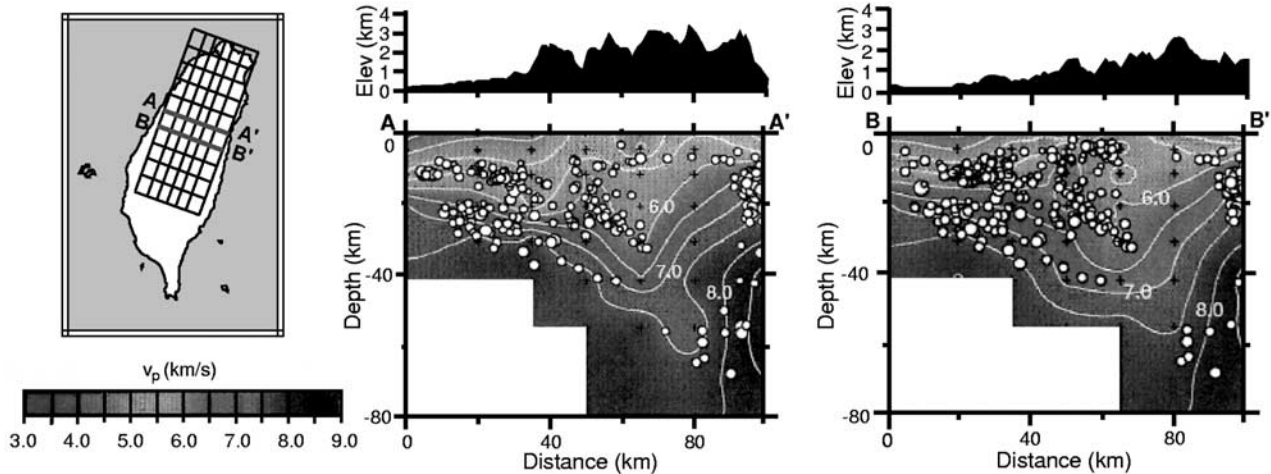
Figure 13. Regional tomography adapted from *Rau and Wu* [1995] (with permission from Elsevier Science). A well-resolved high-velocity feature comparable to the one found for the PSP at the Ryukyu Trench can be observed underneath the Coastal Range and eastern Central Range. The Central Range is underlain by a region of high velocity. See color version of this figure in the HTML.

development of the region. East of present-day Taiwan, the subduction of the PSP below the Chinese continental margin in the past million years has been characterized by tearing of the continental-ocean boundary (COB) in roughly WSW direction. The tear consistently followed the geometry of the COB, thereby progressively creating the west Ryukyu Trench [*Lallemand et al.*, 2001]. This westward migration of incipient PSP subduction is caused by the obliqueness of the PSP motion relative to the strike of the Eurasian plate. Trench creation thus advanced with an average speed comparable to the component of PSP motion along the strike of the COB. The position of the tear tip coincides with the northern extent of the (more or less N-S striking) Manila trench, which accommodates EUP subduction up to this latitude [*Lallemand et al.*, 2001]. In the past 3–5 Myr the strike of the Ryukyu trench has aligned with the relative motion of the PSP. When viewed in a Eurasian fixed reference frame, the EUP has been rolling back to the west while the component of the PSP motion along strike of the COB (or normal to the Manila trench) provides the overriding motion. As long as roll-back speed and overriding motion are equal there is no special reason for strong orogenic activity. The Taiwan orogen itself must then result from a change in the difference between roll-back speed of the EUP and the westward component of PSP advance. We believe that the Taiwan orogen is a direct result of a strong southward turn of the strike of the Chinese continental margin, which existed east of Taiwan. Ongoing roll-back of the Manila trench now brings the COB in the position of being overridden by the PSP [*Chai*, 1972; *Suppe*, 1981, 1984; *Tsai*, 1986]. Resistance of the Chinese continental lithosphere to subduction has decreased the roll-back motion causing the PSP to indent the Chinese continental margin thus creating an accretionary wedge, the Taiwan orogen. The decrease in slab roll-back also led to a steepening of the dip of the EUP, as observed in the global tomography (Figure 10). Subsequently part of the continental crust subducted to midcrustal levels before buoyancy forces initiated failure and thickening of the subducting

crust along two conjugate thrust faults resulting in the exhumation (squeezing out) of a crustal slice [*Chemenda et al.*, 2001] as we have deduced for the eastern Central Range. Further, the Ryukyu trench has not propagated into the Chinese continental margin (hence is not tearing the continent as exemplified by the "T1 tear" of *Lallemand et al.* [2001]). Instead, we propose the southward propagation (more of less along the east coast of Taiwan) of the Ryukyu
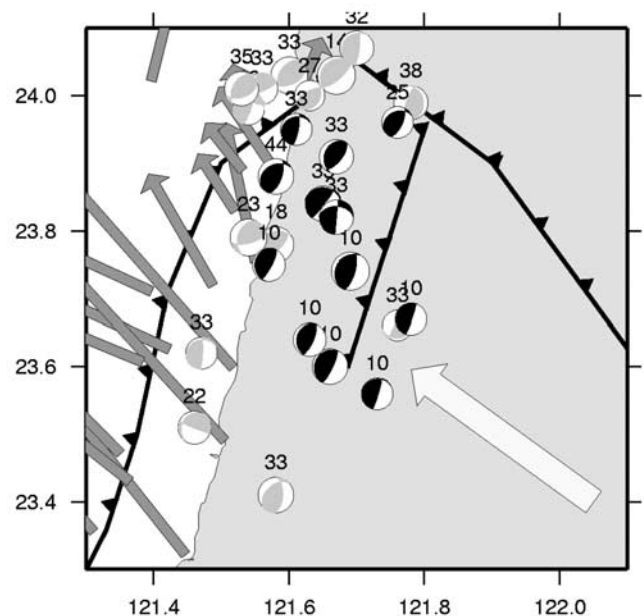

Figure 14. Focal mechanisms from the Harvard CMT catalog (*M* > 4, depth < 50 km). Solid mechanisms all denote a fault with a strike of 23°N and dip of 73° with the horizontal. The grey vectors denote the GPS velocity vectors of *Yu et al.* [1997]. The open vector represents the PSP motion. Barbed lines represent the Ryukyu trench where the central segment denotes our proposed southward continuation.

trench, thus overcoming the jog in the COB geometry below present-day Taiwan. In conjunction with this southward bending of the trench incipient northwestward subduction of the PSP under Taiwan is now in progress.

9. Summary and Conclusions

[44] The method of *Spakman and Nyst* [2002] has been applied to derive the surface deformation from GPS motion vectors, where we explored different modeling options. The fault slip-only solution of inversion I results in large data misfits and the agreement with neotectonic fault observations is poor. The solution in terms of $\nabla\mathbf{v}$ generates smaller data misfits. This model generally agrees with other continuous-deformation-only studies. However, the presence of large, active faults on Taiwan cannot be ignored; thus the kinematics of Taiwan should be studied in terms of fault slip and $\nabla\mathbf{v}$.

[45] Inversion III provides an acceptable data misfit, covariance and spatial resolution. In this model the method of *Spakman and Nyst* [2002] exposes a trade-off problem between fault slip and the velocity gradient field that can only be resolved by placing both stations close to the faults and stations in the interior of crustal blocks. The model shows significant motion on the Longitudinal Valley fault, the southern Chukou fault, and the southern Deformation Front. Strain rates rotate from NW-SE contraction in the Coastal Range to E-W contraction in the southern Western Foothills and NW-SE extension in northern Taiwan. The rotation rate field shows several blocks with consistent (anti) clockwise rotation.

[46] The interpretation of our surface deformation model, combined with the seismicity data, gravity data and tomography leads to a coherent model for the present-day tectonic activity of Taiwan (Figure 11). We divide Taiwan in four distinct domains: southern Taiwan, central Taiwan, northern Taiwan, and the Coastal Range. The domains are bounded by the two major transfer fault zones and the Longitudinal Valley fault. We deduce active convergence between the EUP and the PSP in both central and southern Taiwan. In southern Taiwan the almost E-W collision has resulted in N-S lateral extrusion of the weak sedimentary cover toward the Manila accretionary wedge. To the north the extrusion is terminated by the Chishan Transfer Fault zone. In our deformation model the eastern Central Range of central Taiwan obtains almost orogen perpendicular extension, while the western Central Range and the Western Foothills show predominantly NW-SE collision induced contraction. In conjunction with *Chemenda et al.* [2001], *Lin* [1998], and *Lin et al.* [1998] we relate this feature to active exhumation of a crustal slice. However, we believe that the exhumation is propagating southward along with the collision, causing the principle directions of the extension to rotate to a more NE-SW orientation. Northern Taiwan is transferring into a state of gravitational collapse induced by the inland propagation of the opening Okinawa Trough [*Liu*, 1995b; *Yeh et al.*, 1989] along a preexisting weak zone, the Lishan fault. Though our model shows that south of 23.5°N a very significant part of the convergence between the PSP and the South China Sea is accommodated by slip on the Longitudinal Valley fault, north of 23.5°N about 40–50 mm yr^{-1} needs to be accommodated east of the island of Taiwan. We observe a clear northwestward

dipping Wadati-Benioff zone in both the seismicity data and the regional tomographic model of *Rau and Wu* [1995]. We deduce that in the transfer zone between the two contrary subduction zones a southward propagating crustal tear fault has developed east of Taiwan. The tear fault is the crustal response to incipient northwestward subduction of the PSP below eastern Taiwan. Thus the Ryukyu trench is bending southward becoming almost perpendicular to the convergence direction, while subduction of the PSP continues. Slab-slab interaction between the PSP slab and the Eurasian slab may occur and detachment of the Eurasian slab may commence. In this setting a sudden rapid southward propagation of incipient subduction is conceivable.

References

Angelier, J., F. Bergerat, H.-T. Chu, and T.-Q. Lee, Tectonic analysis and the evolution of a curved collision belt: The Hsuehshan Range, northern Taiwan, *Tectonophysics*, *183*, 77–96, 1990.

Angelier, J., H.-T. Chu, and J.-C. Lee, Shear concentration in a collision zone: Kinematics of the Chihshang fault as revealed by outcrop-scale quantification of active faulting, Longitudinal Valley, eastern Taiwan, *Tectonophysics*, *274*, 117–143, 1997.

Angelier, J., H.-T. Chu, J.-C. Lee, and J.-C. Hu, Active faulting and earthquake risk: The Chihshang Fault case, Taiwan, *J. Geodyn.*, *29*, 151–185, 2000.

Barr, T. D., and F. A. Dahlen, Constraints on friction and stress in the Taiwan fold-and-thrust belt from heat flow and geochronology, *Geology*, *18*, 111–115, 1990.

Barrier, E., and J. Angelier, Active collision in eastern Taiwan: The Coastal Range, *Tectonophysics*, *125*, 39–72, 1986.

Beavan, J., and J. Haines, Contemporary horizontal velocity and strain rate fields of the Pacific-Australian plate boundary zone through New Zealand, *J. Geophys. Res.*, *106*, 741–770, 2001.

Bennett, R. A., W. Rodi, and R. E. Reilinger, Global Positioning System constraints on fault slip rates in southern California and northern Baja, Mexico, *J. Geophys. Res.*, *101*, 21,943–21,960, 1996.

Bijwaard, H., and W. Spakman, Non-linear global *P*-wave tomography by iterated linearized inversion, *Geophys. J. Int.*, *141*(1), 71–82, 2000.

Bijwaard, H., W. Spakman, and R. Engdahl, Closing the gap between regional and global travel time tomography, *J. Geophys. Res.*, *103*, 30,055–30,078, 1998.

Biq, C. C., Dual trench structure in the Taiwan-Luzon region, *Proc. Geol. Soc. China*, *15*, 65–75, 1972.

Chai, B. H. T., Structure and tectonic evolution of Taiwan, *Am. J. Sci.*, *272*, 389–422, 1972.

Chemenda, A. I., R.-K. Yang, C.-H. Hsieh, and A. L. Groholsky, Evolutionary model for the Taiwan collision based on physical modeling, *Tectonophysics*, *274*, 253–274, 1997.

Chemenda, A. I., R.-K. Yang, J.-F. Stephan, E. A. Konstantinovskaya, and G. M. Ivanov, New results from physical modeling of arc-continent collision in Taiwan: Evolutionary model, *Tectonophysics*, *333*, 159–178, 2001.

Chen, H., Crustal uplift and subsidence in Taiwan: An account based on retriangulation results (in Chinese), *Spec. Publ. Cent. Geol. Surv.*, *3*, 127–140, 1984.

Crespi, J. M., T.-K. Liu, S. Hsieh, C.-Y. Lu, and C.-H. Chen, Structural and thermal evidence for extension in the high elevations of Taiwan, *Eos Trans. AGU*, *71*(43), 1618, 1990.

Crespi, J. M., Y. C. Chan, and M. S. Swaim, Synorogenic extension and exhumation of the Taiwan hinterland, *Geology*, *24*, 247–250, 1996.

Dahlen, F. A., Critical taper model of fold-and-thrust belts and accretionary wedges, *Annu. Rev. Earth Planet. Sci.*, *18*, 55–99, 1990.

Deffontaines, B., O. Lacombe, J. Angelier, H.-T. Chu, F. Mouthereau, C.-T. Lee, J. Deramond, J.-F. Lee, M.-S. Yu, and P. M. Liew, Quaternary transfer faulting in the Taiwan Foothills: Evidence from a multisource approach, *Tectonophysics*, *274*, 61–82, 1997.

Ellwood, A., C.-Y. Wang, L. S. Teng, and H.-Y. Yen, Gravimetric examination of thin-skinned detachment vs. basement-involved models for the Taiwan orogen, *J. Geol. Soc. China*, *39*, 209–221, 1996.

Herman, B. M., R. N. Anderson, and M. Truchan, Extensional tectonics in the Okinawa Trough, in *Geological and Geophysical Investigations of Continental Margins*, edited by J. Watkins, I. Montadert, and P. Dickinson, *AAPG Mem.*, *29*, 199–208, 1978.

Ho, C. S., An introduction to the geology of Taiwan, technical report, 2nd ed., 92 pp., Cent. Geol. Surv., Minist. of Econ. Affairs, Taipei, 1988.

Hsieh, S. H., and C. C. Hu, Gravimetric and magnetic studies of Taiwan, *Pet. Geol. Taiwan*, *10*, 283–321, 1972.

Hu, J.-C., J. Angelier, J.-C. Lee, H.-T. Chu, and D. Byrne, Kinematics of convergence, deformation and stress distribution in the Taiwan collision area: 2-D finite-element numerical modeling, *Tectonophysics*, *255*, 243–268, 1996.

Hu, J.-C., J. Angelier, and S.-B. Yu, An interpretation of the active deformation of southern Taiwan based on numerical simulation and GPS studies, *Tectonophysics*, *274*, 145–169, 1997.

Hwang, W.-T., and C.-Y. Wang, Sequential thrusting model for mountain building: Constraints from geology and heat flow of Taiwan, *J. Geophys. Res.*, *98*, 9963–9973, 1993.

Kahle, H.-G., M. Cocard, Y. Peter, A. Geiger, R. Reilinger, A. Barka, and G. Veis, GPS-derived strain rate field within the boundary zones of the Eurasian, African, and Arabian plates, *J. Geophys. Res.*, *105*, 23,353–23,370, 2000.

Kao, H., S.-S. J. Shen, and K.-F. Ma, Transition from oblique subduction to collision: Earthquakes in the southernmost Ryukyu arc-Taiwan region, *J. Geophys. Res.*, *103*, 7211–7229, 1998.

Kimura, M., Back-arc rifting in the Okinawa Trough, *Pet. Geol.*, *2*, 222–240, 1985.

Kosuga, M., H. Sato, T. Tanaka, and H. C. Shue, Crustal movement along a collision boundary of plates (case of eastern Taiwan), *J. Geodyn.*, *10*, 189–205, 1988.

Lacombe, O., F. Mouthereau, B. Deffontaines, J. Angelier, H. T. Chu, and C. T. Lee, Geometry and Quartenary kinematics of fold-and-thrust units in southwestern Taiwan, *Tectonics*, *18*, 1198–1223, 1999.

Lacombe, O., F. Mouthereay, J. Angelier, and B. Deffontaines, Structural, geodetic and seismological evidence for tectonic escape in SW Taiwan, *Tectonophysics*, *333*, 323–345, 2001.

Lallemand, S., C.-S. Liu, and Y. Font, A tear fault boundary between the Taiwan orogen and the Ryukyu subduction zone, *Tectonophysics*, *274*, 171–190, 1997.

Lallemand, S., Y. Font, H. Bijwaard, and H. Kao, New insights on 3-D plates interaction near Taiwan from tomography and tectonic implications, *Tectonophysics*, *335*, 229–253, 2001.

Lee, J.-C., and J. Angelier, Localisation des déformations actives et traitement des données géodésiques: L'exemple de la faille de la Vallée Longitudinale, Taïwan, *Bull. Soc. Geol. Fr.*, *164*, 533–543, 1993a.

Lee, J.-C., J. Angelier, and H.-T. Chu, Polyphase history and kinematics of a complex major fault zone in the northern Taiwan mountain belt: The Lishan fault, *Tectonophysics*, *274*, 97–116, 1997.

Lee, J.-C., J. Angelier, H.-T. Chu, J.-C. Hu, and F.-S. Jeng, Continuous monitoring of an active fault in a plate suture zone: A creepmeter study of the Chihshang fault, eastern Taiwan, *Tectonophysics*, *333*, 219–240, 2001.

Lee, T.-Q., Preliminary paleomagnetic study on lake sediments at Yuashan, Ilan, northeastern Taiwan, *Bull. Inst. Earth Sci.*, *13*, 46–50, 1993b.

Lee, T.-Q., J. Angelier, H.-T. Chu, and F. Bergerat, Rotations in the northeastern collision belt of Taiwan: Preliminary results from paleomagnetism, *Tectonophysics*, *199*, 109–120, 1991.

Lewis, S. D., and D. E. Hayes, The tectonics of northward propagating subduction along eastern Luzon, Philippine Islands, in *The Tectonic and Geologic Evolution of Southeast Asian Seas and Islands: Part 2*, *Geophys. Monogr. Ser.*, vol. 27, edited by D. E. Hayes, pp. 57–78, AGU, Washington, D. C., 1983.

Lin, C.-H., Tectonic implications of an aseismic belt beneath the eastern Central Range of Taiwan: Crustal subduction and exhumation, *J. Geol. Soc. China*, *41*, 441–460, 1998.

Lin, C.-H., Y.-H. Yeh, H.-Y. Yen, K.-K. Chen, and B.-S. Huang, Three-dimensional elastic wave velocity structure of the hualien region of Taiwan: Evidence of active crustal exhumation, *Tectonics*, *17*, 89–103, 1998.

Lin, M. T., and Y. B. Tsai, Seismotectonics in Taiwan-Luzon area, *Bull. Inst. Earth Sci.*, *1*, 51–82, 1981.

Liu, C., Geodetic monitoring of mountain building in Taiwan, *Eos Trans. AGU*, *76*(46), Fall Meet. Suppl., F636, 1995a.

Liu, C.-C., The Ilan Plain and the southwestward extending Okinawa Trough, *J. Geol. Soc. China*, *38*, 229–242, 1995b.

Lu, C.-Y., and J. Malavieille, Oblique convergence, indentation and rotation tectonics in the Taiwan mountain belt: Insights from experimental modeling, *Earth Planet. Sci. Lett.*, *121*, 477–494, 1994.

Lu, C.-Y., S.-B. Yu, and H.-T. Chu, Neotectonics of the Taiwan mountain belt, in *Mantle Dynamics and Plate Interactions in East Asia*, *Geodyn. Ser.*, vol. 27, edited by M. Fowler et al., pp. 301–315, AGU, Washington, D. C., 1998.

Miki, M., M. Furkawa, Y. Otofuji, S. Tsao, and T. Huang, Paleomagnetism and K-Ar ages of Neogene rocks of northern Taiwan: Tectonics of the arc junction of Ryukyu and Luzon arcs, *Geophys. J. Int.*, *114*, 225–233, 1993.

Nyst, M. C. J., A new approach to model the kinematics of crustal deformation with application to the Aegean and Southeast Asia, Ph.D. thesis, Tech. Univ. of Delft, Delft, Netherlands, 2001.

Rau, R.-J., 3-D seismic tomography, focal mechanisms and Taiwan orogeny, Ph.D. thesis, State Univ. of N. Y., Binghamton, 1996.

Rau, R.-J., and F. T. Wu, Tomographic imaging of lithospheric structures under Taiwan, *Earth Planet. Sci. Lett.*, *133*, 517–532, 1995.

Rocher, M., O. Lacombe, J. Angelier, and H.-W. Chen, Mechanical twin sets in calcite markers of recent collisional events in a fold-and-thrust belt: Evidence from the reefal limestones of southwestern Taiwan, *Tectonics*, *15*, 984–996, 1996.

Seno, T., S. Stein, and A. E. Gripp, A model for the motion of the Phillipine Sea Plate consistent with NUVEL-1 and geological data, *J. Geophys. Res.*, *98*, 17,941–17,948, 1993.

Shewchuk, J., Triangle: Engineering a 2D quality mesh generator and Delaunay triangulator, paper presented at First Workshop on Applied Computational Geometry, Assoc. for Comput. Mach., Philadelphia, Pa., 1996.

Sibuet, J.-C., J. Letouzey, J. Charvet, J.-P. Foucher, T. W. C. Hilde, M. Kimura, C. Ling-Yun, B. Marsset, C. Muller, and J.-F. Stephan, Back arc extension in the Okinawa Trough, *J. Geophys. Res.*, *92*, 14,041–14,063, 1987.

Spakman, W., and M. C. J. Nyst, Inversion of relative motion data for fault slip and continuous deformation in crustal blocks, *Earth Plan. Sci. Lett.*, *203*, 577–591, 2002.

Suppe, J., Mechanics of mountain building and metamorphism in Taiwan, *Mem. Geol. Soc. China*, *4*, 67–89, 1981.

Suppe, J., Kinematics of arc-continent collision, flipping of subduction, and back-arc spreading near Taiwan, *Mem. Geol. Soc. China*, *6*, 21–33, 1984.

Teng, L. S., Geotectonic evolution of late Cenozoic arc-continent collision, *Tectonophysics*, *183*, 57–76, 1990.

Teng, L. S., Extensional collapse of the northern Taiwan mountain belt, *Geology*, *24*, 949–952, 1996.

Teng, L. S., C. T. Lee, Y. B. Tsai, and L.-Y. Hsiao, Slab breakoff as a mechanism for flipping of subduction polarity in Taiwan, *Geology*, *28*, 155–158, 2000.

Tsai, Y. B., Seismotectonics of Taiwan, *Tectonophysics*, *125*, 17–37, 1986.

Van de Zedde, D. M. A., and M. J. R. Wortel, Shallow slab detachment as a transient source of heat at midlithospheric depths, *Tectonics*, *20*, 868–882, 2001.

Wdowinski, S., Y. Sudman, and Y. Bock, Geodetic detection of active faults in southern California, *Geophys. Res. Lett.*, *28*, 2321–2324, 2001.

Wong A Ton, S. Y. M., and M. J. R. Wortel, Slab detachment in continental collision zones: An analysis of controlling parameters, *Geophys. Res. Lett.*, *24*(16), 2095–2098, 1997.

Wortel, M. J. R., and W. Spakman, Structure and dynamics of subducted lithosphere in the Mediterranean region, *Proc. K. Ned. Akad. Wetensch.*, *95*, 325–347, 1992.

Wortel, M. J. R., and W. Spakman, Subduction and slab detachment in the Mediterranean-Carpathian region, *Science*, *290*, 1910–1917, 2000.

Wu, F. T., R.-J. Rau, and D. Salzberg, Taiwan orogeny: Thin skinned or lithosperic collision?, *Tectonophysics*, *274*, 191–220, 1997.

Yeh, Y.-H., C.-H. Lin, and S. W. Roecker, A study of upper crustal structures beneath northeastern Taiwan: Possible evidence of the western extension of Okinawa Trough, *Proc. Geol. Soc. China*, *32*, 139–156, 1989.

Yen, H.-Y., Y.-H. Yeh, and F. T. Wu, Two-dimensional crustal structures of Taiwan from gravity data, *Tectonics*, *17*, 104–111, 1998.

Yu, S.-B., and H. Y. Chen, Strain accumulation in southwestern Taiwan, *TAO*, *9*, 31–50, 1998.

Yu, S.-B., and L. C. Kuo, Present-day crustal motion along the Longitudinal Valley fault, eastern Taiwan, *Tectonophysics*, *333*, 199–218, 2001.

Yu, S.-B., D. D. Jackson, G. K. Yu, and C. C. Liu, Dislocation model for crustal deformation in the Longitudinal Valley area, eastern Taiwan, *Tectonophysics*, *183*, 97–109, 1990.

Yu, S.-B., H. Y. Chen, and L. C. Kuo, Velocity field of GPS stations in the Taiwan area, *Tectonophysics*, *274*, 41–59, 1997.

————————————

A. G. Bos and W. Spakman, Faculty of Earth Sciences, Utrecht University, Budapestlaan 4, 3584 CD Utrecht, Netherlands. (bos@geo.uu.nl; wims@geo.uu.nl)

M. C. J. Nyst, U.S. Geological Survey, 345 Middlefield Road, MS 977, Menlo Park, CA 94025, USA. (mnyst@usgs.gov)